TU Delft

Delft University of Technology

Tidally induced lateral variations of Io's interior

Steinke, T.; Hu, H.; Höning, D.; van der Wal, W.; Vermeersen, B.

DOI
10.1016/j.icarus.2019.05.001

Publication date
2020

Document Version
Final published version

Published in
Icarus

Citation (APA)
Steinke, T., Hu, H., Höning, D., van der Wal, W., & Vermeersen, B. (2020). Tidally induced lateral variations of Io's interior. *Icarus*, *335*, Article 113299. https://doi.org/10.1016/j.icarus.2019.05.001

Important note
To cite this publication, please use the final published version (if applicable).
Please check the document version above.

Copyright
Other than for strictly personal use, it is not permitted to download, forward or distribute the text or part of it, without the consent of the author(s) and/or copyright holder(s), unless the work is under an open content license such as Creative Commons.

Takedown policy
Please contact us and provide details if you believe this document breaches copyrights.
We will remove access to the work immediately and investigate your claim.

This work is downloaded from Delft University of Technology.
For technical reasons the number of authors shown on this cover page is limited to a maximum of 10.

Green Open Access added to TU Delft Institutional Repository

'You share, we take care!' - Taverne project

https://www.openaccess.nl/en/you-share-we-take-care

Otherwise as indicated in the copyright section: the publisher is the copyright holder of this work and the author uses the Dutch legislation to make this work public.

Icarus 335 (2020) 113299

Contents lists available at ScienceDirect

Icarus

journal homepage: www.elsevier.com/locate/icarus

Tidally induced lateral variations of Io's interior

T. Steinke[a,*], H. Hu[a], D. Höning[b,c], W. van der Wal[a], B. Vermeersen[a]

[a] Faculty of Aerospace Engineering, Delft University of Technology, Delft, the Netherlands
[b] Origins Center, Groningen, the Netherlands
[c] Department of Earth- and Life Sciences, Vrije Universiteit Amsterdam, Amsterdam, the Netherlands

ARTICLE INFO

Keywords:
Tidal dissipation
Io
Heterogeneous internal heating
Mantle convection
Melt advection

ABSTRACT

Satellite and recent Earth-based observations of Io's surface reveal a specific spatial pattern of persisting hotspots and sudden high-intensity events. Io's major heat producing mechanism is tidal dissipation, which is thought to be non-uniformly distributed within Io's mantle and asthenosphere. The question arises to what extent Io's non-homogeneous heat production can cause long-wavelength variations in the interior and volcanic activity at the surface. We investigate dissipation patterns resulting from two different initially spherical symmetric visco-elastic rheological structures, which are consistent with geodetic observations. The spatial distributions of the time-averaged tidal heat production are computed by a finite element model. Whereas for the first rheological structure heat is produced only in the upper viscous layer (asthenosphere-heating model), the second rheological structure results in a more evenly distributed dissipation pattern (mixed-heating model) with tidal heating occurring in the deep mantle and the asthenosphere. To relate the heat production to the interior temperature and melt distribution, we use steady-state scaling laws of mantle convection and a simple melt migration model. The resulting long-wavelength thermal heterogeneities strongly depend on the initial tidal dissipation pattern, the thickness of the convective layer, the mantle viscosity, and the ratio between magmatic and convective heat transport. While for the asthenosphere-heating model a strong lateral temperature signal with up to 190 K peak-to-peak difference can remain, convection within a thick convective layer, as for the mixed-heating model, can reduce the lateral temperature variation to < 1 K, if the mantle viscosity is sufficiently low. Models with a dominating magma heat transport preserve the long-wavelength pattern of tidal dissipation much better and are favoured, because they are better to explain Io's thick crust. The approach presented here can also be applied to investigate the effect of an arbitrary interior heating pattern on Io's volcanic activity pattern.

1. Introduction

Unlike any of the other satellites in the Solar System that we know Io shows signs of active silicate volcanism (Carr, 1986; McEwen et al., 1998). In contrast to terrestrial planets with recent or active silicate volcanism, Io's present heat output is not due to remnant cooling, but due to extreme and non-uniform tidal heating (Beuthe, 2013; Ross et al., 1990; Segatz et al., 1988). Because of this uniqueness within the Solar System, Io serves as a potential archetype of rocky exoplanets and exomoons undergoing extreme tidal heating. Understanding Io's recent cooling processes could provide insight into the early evolution of the terrestrial planets, when they were still hotter and possibly had a similar heat flux as Io has today.

Io's observed volcanic activity is an important link to help understanding the satellite's interior processes. The non-uniform volcanic pattern is commonly associated with a radial heat flux originating from Io's non-uniform long-wavelength heat production pattern (Davies et al., 2015; Hamilton et al., 2013; Ross et al., 1990). However, the complex interplay of Io's internal heat transport mechanism and physical properties makes the assumption of a purely radial heat flow questionable.

The distinct heat production distribution depends in an intricate way on the tidal perturbation and rheology of Io's interior (Beuthe, 2013). Several studies based on the physics of solid visco-elastic material have been conducted (Bierson and Nimmo, 2016; Ross et al., 1990; Segatz et al., 1988) to predict a heat dissipation distribution. Tyler et al. (2015) suggested a dynamic modelling approach by assuming that Io's asthenosphere is a global fluid layer. Both solid and fluid types of models match the strong degree two component that can be found in Io's inferred heat flux maps and Io's global volcanic distribution (Davies et al., 2015; Hamilton et al., 2013). However, whereas the solid model is not able to predict the observed longitudinal shift of

* Corresponding author.
E-mail address: t.steinke@tudelft.nl (T. Steinke).

https://doi.org/10.1016/j.icarus.2019.05.001
Received 11 January 2019; Received in revised form 19 April 2019; Accepted 1 May 2019
Available online 10 May 2019
0019-1035/ © 2019 Elsevier Inc. All rights reserved.

the maxima in the volcanic concentration, the fluid model is not in agreement with the strong volcanic activity at medium latitudes.

Io's interior heat production, heat distribution, and heat transport mechanisms are significantly different from other terrestrial bodies. Io's produced heat is partially transported by convection (Moore et al., 2007). However, due to the extreme heat in Io's interior and low pressures, Io's mantle contains high portions of melt (Khurana et al., 2011). Volcanic channels arise allowing the transport of molten material and heat to the surface, cooling Io's interior more effectively (Bierson and Nimmo, 2016; Elder, 2015; Moore, 2001). Furthermore, dissipative heat forms the most significant part of Io's heat budget as opposed to remnant cooling from the core (Lainey et al., 2009; Peale et al., 1979). Because of the heterogeneous nature of the tidal dissipation pattern, Io's heat is not distributed uniformly in radial and in lateral directions. This leads to a convection system, which cannot be described by scaling laws based on adiabatic temperature profiles and one-dimensional mantle structures as proposed for Mars, Venus and Mercury (Schubert et al., 2001).

Planetary evolution models (Schubert et al., 2001; Spohn, 1991) show that the amount of heat in the interior determines the interior structure of celestial bodies due to the temperature-dependence of the melt fraction and the mantle viscosity. The question arises if a strong non-homogeneous internal heat production, such as for Io, has a lateral varying effect on the interior structure. In this case, Io's interior structure would have a three-dimensional distribution of interior properties, and thus, a possibly different evolving dissipation pattern than derived from radially symmetric structures (Bierson and Nimmo, 2016; Hamilton et al., 2013; Ross et al., 1990; Segatz et al., 1988).

The effect of tidal heating on the interior structure of celestial bodies due to the temperature-dependency of the viscosity has been explored for icy satellites of the outer planetary systems (Ojakangas and Stevenson, 1989; Tobie et al., 2005; Roberts and Nimmo, 2008; Han and Showman, 2010; Běhounková et al., 2010). Terrestrial bodies, however, have been given less attention because of the minor role of tidal dissipation for the terrestrial planets of the Solar System. Běhounková et al. (2010, 2011) investigated the feedback between the heterogeneous rheological structure resulting from mantle convection and the rheology-dependent tidal dissipation in a three-dimensional numerical model for Earth-like exoplanets. However, because their investigations are based on different orbital and interior properties their conclusions cannot be applied to Io. Studies focusing on Io have been conducted by Tackley (2001), Tackley et al. (2001) and Bierson and Nimmo (2016). The first two studies investigate the effect of the three-dimensional heating pattern on the temperature structure and lateral heat flux pattern for a purely convective asthenosphere and mantle. This approach possibly underestimates the effect of tidally induced heating on the heat flux pattern, as it neglects advection of melt. This heat removal mechanism transports heat more quickly and maintains a more radial direction. In contrast, Bierson and Nimmo (2016) derived a three-dimensional melt distribution based on the assumption that the lateral varying produced heat is exclusively transported by magma. This approach, however, possibly overestimates the tidal-dissipation induced signal on the surface heat flux pattern, as lateral flow due to mantle convection is neglected. We suggest that a combination of convective and magmatic heat transport would improve the estimations of tidally induced variations of Io's surface heat flux and volcanic activity pattern.

In this paper we aim to explore whether Io's heterogeneous heating causes lateral variations of the internal structure or whether the assumption of a well-mixed radially symmetric mantle is justified. To achieve that we combine heterogeneous tidal heat dissipation with a coupled system of mantle convection and advection of melt. Further, we link our modelling results to observables, such as Io's surface pattern of volcanic features (Davies et al., 2015; Kirchoff et al., 2011; de Kleer and de Pater, 2016; Veeder et al., 2015). We focus on first-order effects of the tidal dissipation pattern on the interior. To model Io's convective mantle we use a steady-state scaling law and ignore small-scale anomalies triggered by mantle convection as they are difficult to predict. Thus, our resulting long-wavelength patterns can be seen as a statistically averaged solution.

Since our main aim is to explore the relation between the tidal dissipation patterns and the tidal-dissipation-induced lateral variations we do not explore the full range of possible dissipation patterns. Instead, we investigate two end-members of possible tidal dissipation pattern based on Ross et al. (1990). We choose to compute the tidal dissipation with a numerical finite element (FE) model that can deal with three-dimensional variations of the viscosity. In contrast to semi-analytical methods based on a one-dimensional approach (Jara-Orué and Vermeersen, 2011; Sabadini et al., 2016), this allows to calculate the effect of the tidally induced lateral viscosity variations on the tidal dissipation itself in future work.

The FE model and the thermal modelling of Io's interior are introduced in Sections 2 and 3, respectively. In Section 4 we present the resulting lateral maximum temperature and melt distributions for our interior models for a range of model variables. In Section 5 we discuss the influence of the model assumptions on the obtained results and the implications of our results on the interpretation of Io's volcanic surface features.

2. Numerical modelling of volumetric tidal heating

In this section the three components of the numerical model for the volumetric tidal heating are introduced and discussed: 1) the periodic tidal forcing, 2) the solution of the equation of motion, here implemented in a finite element (FE) model, and 3) the rheological model and the choice of the interior properties.

2.1. Periodic tidal forcing

Io's eccentric orbit causes periodic variations of the distance between Io and Jupiter, and also causes differences between the rotation velocity and orbital velocity of the satellite. The potential due to the 1:1 spin-orbit resonance at a point is given as a function of the time t, and the spherical coordinates of the point, i.e. the radial distance from the centre of Io r, and the longitude ϕ and co-latitude θ (Kaula, 1964):

$$V_p(t,r,\theta,\phi) = \omega^2 r^2 e\left(\frac{3}{2}P_{2,0}(\cos\theta)\cos(\omega t) - \frac{3}{4}P_{2,2}(\cos\theta)\cos(2\phi)\cos(\omega t) - P_{2,2}(\cos\theta)\sin(2\phi)\sin(\omega t)\right), \quad (1)$$

where $\omega = 2\pi/P_{orbit}$ is the mean motion with P_{orbit} the orbital period of Io, and e the eccentricity of Io's orbit. $P_{2,0}(\cos\theta)$ and $P_{2,2}(\cos\theta)$ are the degree two associated Legendre polynomials of order zero and two, respectively. The inclination of Io's rotation axis and physical librations are unknown but expected to be small (Yoder and Peale, 1981). Thus, their effects on the dissipation pattern (Beuthe, 2013; Frouard and Efroimsky, 2017) are neglected. Furthermore, we assume that Io is fully relaxed under every static force and neglect the effect of any static bulge of the body on the periodic tidal response. The geophysical and geodetic parameters used to describe the strength and the period of the tidal forcing for Io are presented in Table 1.

2.2. Finite element approach

We solve the equation of motion using a finite element model (ABAQUS version 6.14) and follow the method of Wu (2004) to account for self-gravitation in an iterative way. The FE model was developed by Hu et al. (2017) to calculate the change of the moment of inertia tensor for non-spherical symmetric bodies. For this study, the model is used to calculate the effect of periodic tidal forces (Eq. (1)) on Io's interior.

The FE model solves for the deformation field u for each time step, following the conservation of mass

Table 1
Geophysical and geodetic parameters of Io taken from (1) Anderson et al. (2001), (2) Lissauer and De Pater (2013), and (3) Lainey et al. (2009).

Parameter	Notation	Value	Unit
Mean density[(1)]	ρ	3527.8	$kg\,m^{-3}$
Mean radius[(1)]	R	1821.6	km
Eccentricity[(2)]	e	0.0041	–
Normalized moment of inertia[(1)]	C/MR^2	0.37685	–
Orbital period[(2)]	P_{orbit}	1.769138	days
Imaginary part of Love number[(3)]	$-\mathrm{Im}(\widetilde{k_2})$	0.015	–

$$\nabla \cdot u = 0, \tag{2}$$

and the conservation of momentum

$$\nabla \cdot \sigma + f = 0, \tag{3}$$

where f is the body force applied as a surface load at boundaries between the layers of different densities. σ is the incremental stress field tensor, including both: the isotropic part of the stress field, controlling the volumetric changes, and the deviatoric part of the stress field, related to any shape changes. The restoring force of isostasy at each boundary of radial change in density is applied following Wu (2004). Any forces due to inertia are neglected. The effect of compressibility is also not included. To include self-gravitation the additional potential due to deformation needs to be included in the body force. The total force that is applied to each boundary at a density jump with a density difference of $\delta\rho$ is consequently described as

$$f = -\delta\rho(\nabla V_p + \nabla\Lambda), \tag{4}$$

where V_p is the external tidal potential given in Eq. (1) and Λ is the potential of the perturbation of the gravity field. The latter perturbation arises due to the mass redistribution, which is a consequence of the tidal deformation field u. In each iteration step, Λ is re-computed numerically using the deformation field u. The newly calculated load f is applied until the deformation u and stress field σ for each time step t have converged. The number of required iterations depends on the specific problem and is therefore addressed in Appendix B. The type of elements used in the finite element model is important for the stress calculation. Whereas for the deformation and self-gravitation linear elements (8 nodes) deliver sufficient accuracy, the calculation of stresses requires quadratic elements (20 nodes) to account for the non-cubic shape of the elements. However, solving the stress field in the finite element model with quadratic instead of linear elements is a computationally expensive procedure. Therefore, we only apply a quadratic mesh in the final iteration of the self-gravitation iteration.

As the time scale for solid-state convection, modelled in Section 3, is assumed to be much larger than one orbital period, the volumetric tidal heat production is averaged over one orbital period to result in an average three-dimensional tidal dissipation pattern. The average volumetric heat dissipation h_{node} is calculated for each integration point following Hanyk et al. (2005)

$$h_{node} = \frac{1}{P_{orbit}} \int_{\tau}^{\tau+P_{orbit}} \frac{\sigma_D : \sigma_D}{2\eta_{diss}} \mathrm{d}t, \tag{5}$$

where σ_D: σ_D denotes an inner matrix product of the deviatoric stress tensor σ_D, η_{diss} is the viscosity of the visco-elastic mantle at the corresponding integration point, and τ is the time required for the visco-elastic model to adjust to the steady state. Note that since we only use the deviatoric stress field for the calculation of the volumetric dissipation h_{node}, the transformation of the isotropic stress tensor given by Wu (2004) has no effect. The values of the heat dissipation h_{node} are interpolated to an equiangular grid to facilitate spherical harmonic expansion later. The resulting spatial varying internal heating functions $H(r, \phi, \theta)$ are used in Section 3 to calculate the effect of the tidal heat production on Io's interior.

2.3. Rheological model and properties of Io's interior structure

We choose to simulate the visco-elastic behaviour of Io's interior with the Maxwell rheology. The Maxwell rheology is a very good approximation of the material behaviour for low-frequency loading (Sabadini et al., 2016), and has been applied to Io in previous studies (Hussmann and Spohn, 2004; Ross et al., 1990; Segatz et al., 1988). However, laboratory and geodetic observations show that the Maxwell rheology underestimates the frictional dissipation of a visco-elastic material for perturbations shorter than the Maxwell time of a material (Castillo-Rogez et al., 2011; Efroimsky, 2012). This is the case for realistic rock properties of Io's interior and Io's short tidal perturbation period of about 42 h. For this reason more advanced rheology models, such as the Andrade rheology, have been used for Io by several authors (Bierson and Nimmo, 2016; Makarov and Efroimsky, 2014; Renaud and Henning, 2018). They obtain mantle viscosities that can produce Io's estimated total dissipation $\dot{E}_{total}$ (Lainey et al., 2009) and still allow a solid-state convection.

As suggested by Tobie et al. (2005) we deal with the discrepancy between the viscosity required for the Maxwell rheology and the mantle viscosity by treating the visco-elastic rheology separated from the mantle viscosity associated with solid-state convection. In contrast to the magnitude of the produced heat in each layer, the spatial pattern does not depend on the used viscosity (Beuthe, 2013). Consequently, small differences in the resulting heat flux pattern arise when Andrade rheology instead of Maxwell rheology is used, which, however, do not affect our final conclusions. In the following, we use the term Maxwell viscosity η_{diss} valid for Io's dominating forcing period P_{orbit} when referring to the viscosity used to calculate the dissipation due to internal friction in a visco-elastic medium. In contrast, we use the term mantle viscosity η_{con} for the viscosity that controls the convection of Io's mantle and asthenosphere.

The spatial distribution of heat production is strongly coupled to the rheology properties of the body's interior, i.e. the shear modulus μ, the Maxwell viscosity η_{diss}, and the density distribution ρ. Unfortunately, these parameters cannot be uniquely constrained for Io. A full exploration of possible dissipation patterns is not within the scope of this paper and can be done more efficiently using theoretical considerations such as provided by Beuthe (2013). We instead investigate tidal dissipation patterns resulting from two different interior structure models. The properties of the two models are chosen such that the corresponding initial dissipation patterns result in maximal spatial variations for one model and minimal spatial variations for the other model. Thus, the two models are considered as end-members. Both models have a spherical symmetric structure, as no three-dimensional variations of the interior are known a priori. The structure is composed of a liquid core, a visco-elastic mantle that is divided into a deep high-viscosity layer and a shallow low-viscosity melt containing layer, i.e. the asthenosphere, and a fully elastic crust. In contrast to Segatz et al. (1988) both of our models contain an asthenosphere since observations of Io's interaction with Jupiter's magnetic field suggest a melt containing layer (Khurana et al., 2011). The parameters are selected such that they match with Io's observed mean density, mean radius, the polar moment of inertia provided in Table 1 and Io's observed average surface heat flux of $2.24 \pm 0.45\,W\,m^{-2}$ (Lainey et al., 2009). We select an asthenosphere thickness of 200 km for both models as a compromise between estimates for the thickness of the partially molten layer of several hundreds of kilometres (Bierson and Nimmo, 2016) and estimates of 30 km–50 km (Ross et al., 1990; Segatz et al., 1988). For our FE models we set the crustal thickness to 30 km in agreement with (Turtle et al., 2007) who suggest a range between 10 km and 50 km. The crustal rheology is based on values by Segatz et al. (1988). For the core we take the density of a Fe-FeS eutectic, which is an approximation of the minimal core density (Anderson et al., 2001).

To account for the unknown composition of the deep mantle we investigate a potential interior model of Io with all the heat produced in

Table 2
Common parameters of the rheology and thermal modelling for Model A and Model B following (1) Anderson et al. (2001), (2) Turtle et al. (2007), (3) Segatz et al. (1988), (4) Roberts (1967), and (5) Tackley (2001).

Rheology parameter	Notation	Value	Unit
Core density[(1)]	ρ_c	5150	$kg\,m^{-3}$
Core-mantle boundary	R_{cmb}	965	km
Mantle/crust density	ρ_m	3244	$kg\,m^{-3}$
Crustal thickness[(2)]	$d_{diss,crust}$	30	km
Crustal shear modulus[(3)]	μ_{crust}	$6.5\cdot10^{10}$	Pa
Crustal Maxwell viscosity[(3)]	$\eta_{diss,crust}$	10^{23}	Pa s
Asthenosphere thickness	d_{ast}	200	km

Thermal parameter	Notation	Value	Unit
Mantle thermal conductivity	k_m	3	$W\,m^{-1}\,K^{-1}$
Lid thermal conductivity	k_{lid}	3	$W\,m^{-1}\,K^{-1}$
Grav. acceleration for convection	g	1.7	$m\,s^{-2}$
Surface temperature	T_s	100	K
Thermal diffusivity	κ	10^{-6}	$m^2\,s^{-1}$
Thermal expansivity	α	$2\cdot10^{-5}$	K^{-1}
Critical Rayleigh number[(4)]	$Ra_{H,crit}$	2772	–
Activation energy	E_a	$3\cdot10^5$	$J\,mol^1$
Gas constant	R_{gas}	8.314	$J\,K^{-1}\,mol^{-1}$
Blurring coefficient[(5)]	C	4.413	–
Blurring exponent[(5)]	β	0.2448	–
Reference mantle viscosity	$\bar{\eta}_{con}$	10^{12}–10^{18}	Pa s
Heat flux fraction	$\bar{f}_{cc}$	5–95	%

Table 3
Individual parameters of the rheology and thermal modelling for Model A and Model B.

Rheology parameter	Notation	Model A	Model B	Unit
Deep mantle shear modulus	μ_m	$6\cdot10^{10}$	$2\cdot10^9$	Pa
Deep mantle Maxwell viscosity	$\eta_{diss,m}$	10^{20}	$8\cdot10^{14}$	Pa s
Asthenosphere shear modulus	μ_{ast}	$7.8\cdot10^5$	$9\cdot10^7$	Pa
Asthenosphere Maxwell viscosity	$\eta_{diss,ast}$	10^{11}	$3.5\cdot10^{12}$	Pa s
Mantle heat production ratio	$\dot{E}_m/\dot{E}_{total}$	0	60	%
Asthenosphere heat production ratio	$\dot{E}_{ast}/\dot{E}_{total}$	100	40	%

Thermal parameter	Notation	Model A	Model B	Unit
Thickness of convective layer	d	200	826.6	km
Radius bottom of convective layer	R_{con}	1591.6	965	km
Geometry factor	a_f	0.8925	0.6096	–

the asthenosphere based on Segatz et al. (1988), which we term Model A. We neglect any heat contribution from the deep mantle for Model A (asthenosphere-heating scheme). Thus, the heat production rate in the asthenosphere $\dot{E}_{ast}$ is equal to Io's total heat production rate $\dot{E}_{total}$ but shows large regional variations. For Model B both the asthenosphere and the deep mantle contribute to Io's total heat production. We choose a fraction of 40% asthenosphere-heating and 60% mantle-heating, which leads to a minimisation of regional differences in the spatial heat production pattern at the surface (Ross et al., 1990). The viscosity of the asthenosphere and deep mantle of Model A and B are adjusted in a way to produce the desired heating distribution between the deep mantle and the asthenosphere and Io's total heat production rate $\dot{E}_{total}$. All common parameters defining the rheological structures of Model A and Model B are presented in Table 2. Model A and B specific parameters are presented in Table 3. We calculate the total heat production rate using the macroscopic approach (Beuthe, 2013), which is given as a function of the imaginary part of the complex Love number $\widetilde{k_2}$:

$$\dot{E}_{total} = -\mathrm{Im}\,(\widetilde{k_2})\frac{(\omega R)^5}{G}\frac{21}{2}e^2, \tag{6}$$

with G being the gravitational constant equal to $6.674\cdot10^{-11}\,m^3\,kg^{-1}\,s^{-2}$. The imaginary part of $\widetilde{k_2}$ is given in Table 1 and is obtained by the rheological structures of Model A and Model B using a semi-analytical approach based on normal mode theory (Jara-Orué and Vermeersen, 2011; Sabadini et al., 2016). This semi-analytical method requires much less computational costs as it is based on a one-dimensional description of the interior structure, whereas our FE model is three-dimensional.

3. Thermal modelling

Heat generated by dissipation within Io's interior is transported by thermal diffusion, melt migration, and solid-state convection (Elder, 2015; Moore, 2001; Tackley, 2001). Our aim is to obtain the temperature distribution in the upper layers of the mantle resulting from the spatial pattern of the tidal dissipation taking into account all heat transport mechanisms. The difficulty is that the intensities of the convective, conductive, and magmatic heat transport strongly depend on each other. In the following, we outline our approach to address this problem in order to find a statistically averaged regional solution. For that we make use of scaling laws, which are typically used to analyse the thermal state and evolution of planets and satellites (Fischer and Spohn, 1990; Hussmann and Spohn, 2004; Spohn, 1991; Tosi et al., 2017). Doing so reduces the large number of model parameters. All major steps are presented in Fig. 1.

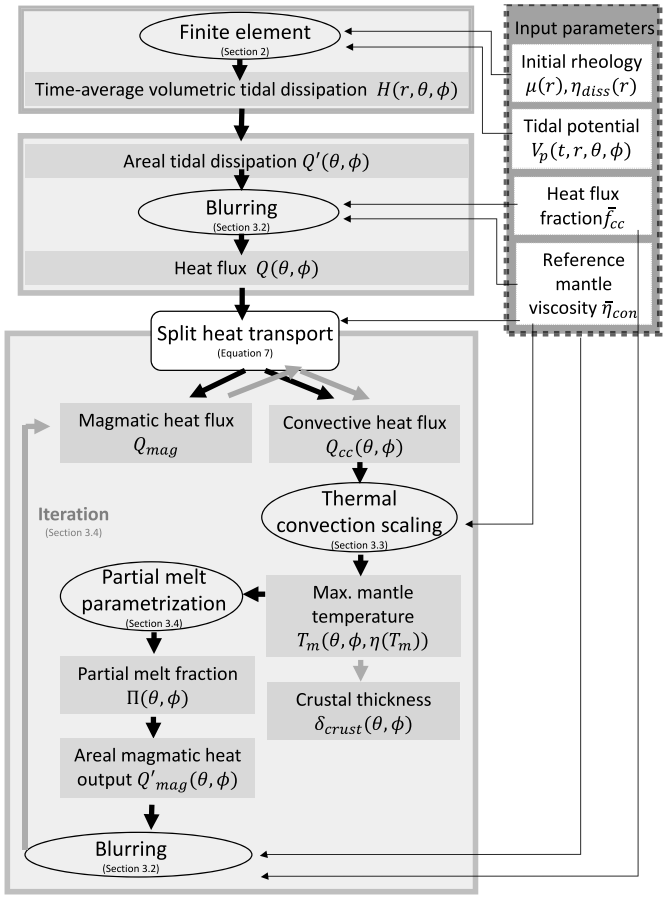

Fig. 1. Flow chart of all modelling steps. Big grey boxes give the three main model steps. The finite element model is described in Section 2, the blurring, the steady-state scaling, and the partial melt parametrisation and the iteration of the local heat flux fluctuation $Q_{cc}(\theta,\phi)$ are presented in Section 3. The dashed box on the right represents the main input parameters, oval boxes give modelling sub-procedures and rectangular boxes display intermediate and final model outputs.

In the first step the three-dimensional volumetric dissipation is projected to Io's surface. The resulting heat production per unit area is then smoothed to account for lateral convective flow. We will refer to this procedure as blurring, as introduced by Tackley (2001). Next, we split the obtained total heat flux $Q(\theta,\phi)$ into a magmatic and a convective-conductive contribution

$$Q(\theta,\phi) = Q_{cc}(\theta,\phi) + Q_{mag}(\theta,\phi), \tag{7}$$

where $Q_{mag}(\theta,\phi)$ is the pattern of the magmatic heat flux and $Q_{cc}(\theta,\phi)$ is the pattern of the convective-conductive heat flux. We treat the fraction

$$\overline{f}_{cc} = \frac{\overline{Q}_{cc}}{\overline{Q}}, \tag{8}$$

between the globally average convective-conductive heat flux $\overline{Q}_{cc}$ and the globally average total heat flux $\overline{Q}$ as a variable. We name this ratio the heat flux fraction. Note that $Q_{mag}(\theta,\phi)$ is related but not equivalent to the observed hot spot heat flow as Io's background heat flow is also fed by intrusive magma (Stevenson and McNamara, 1988). To compute the distribution of the maximum mantle temperature and melt fraction for each longitude ϕ and co-latitude θ we use an analytically derived scaling law from Vilella and Kaminski (2017) to approximate the radial temperature field due to mantle convection. The magmatic heat output $Q'_{mag}(\theta,\phi)$ per unit area is approximated based on the melt fraction and the heat flux fraction $\overline{f}_{cc}$. In the last step, the spatially varying convective-conductive heat flux $Q_{cc}(\theta,\phi)$ is updated keeping $\overline{f}_{cc}$ and the globally average total heat flux $\overline{Q}$ constant (Eq. (7)). The last steps are repeated several times (see Fig. 1) until $Q_{cc}(\theta,\phi)$ converges and an equilibrium mantle temperature, melt fraction and magmatic heat output are found.

In the following we give a general description of a volumetric heated system (Section 3.1) before we describe the different steps of the above introduced model procedure: the blurring of Io's produced heat (Section 3.2), the approximation of the mantle temperature (Section 3.3), and the inclusion of the laterally varying magmatic heat transport and the iteration scheme (Section 3.4).

3.1. Steady-state scaling of a volumetric heated convective system

Io is intensively heated from within the mantle. Its heat flux is > 100 times larger than the heat flux of Earth's moon (Langseth et al., 1976). Therefore, radioactive decay and remnant heat play a minor role for Io's heat budget. For this study, it is therefore assumed that the net heat flux from the core to the mantle is zero (Tackley et al., 2001). We assume that Io's mantle is incompressible, convective, and separated from the surface by a stagnant lid (Moore, 2003). Furthermore, we assume that the heat production rate is equal to the heat loss of the system as shown for Io by Lainey et al. (2009). Scaling laws for internally heated Cartesian systems in a thermal steady state have been investigated numerically (Parmentier and Sotin, 2000; Parmentier et al., 1994; Vilella and Kaminski, 2017) and by laboratory experiments (Limare et al., 2015). Both types of experiments show that in a volumetric heated system active down-welling with passive up-welling occurs. This leads to a sub-adiabatic geotherm as schematically shown in Fig. 2. Thus, the maximum temperature within the convective system can be found at the bottom of the thermal boundary layer, which is a thin layer below the stagnant lid. The thermal boundary is still a part of the convective layer, according to the used scaling law, although its temperature profile is conductive. We assume that the heat transport by magma is proportional to the maximum melt fraction. Consequently, knowledge of the slope of the adiabat is not required. However, the used scaling law for mantle convection does not account for the presence of melt, thus it is implicitly assumed that melt and heat are removed immediately, without interfering with the mantle convection. To estimate the maximum temperature specific parameters of the convective system, such as the temperature increase across the convective

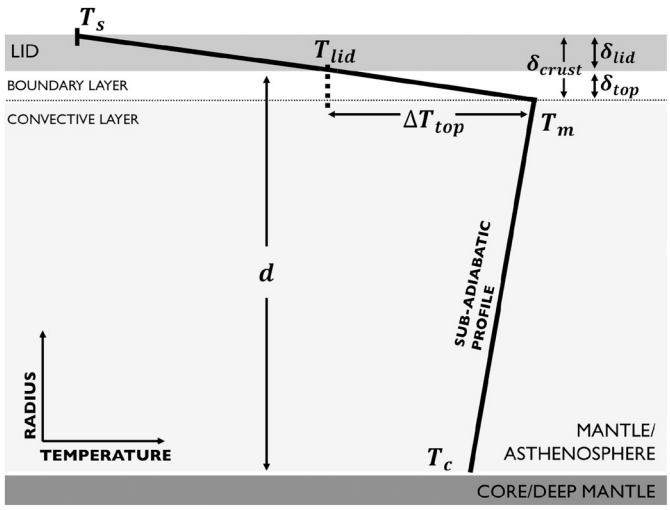

Fig. 2. Schematic temperature profile of Io. The geotherm is plotted in a Cartesian system of the radius and temperature. In the modelling we correct for the spherical geometry.

layer and the strength of convection, the Rayleigh-Roberts number is required. This will be briefly introduced here. In a purely internally heated system the temperature jump across the convective layer ΔT_H can be non-dimensionalized using a volumetric heat production scale (Schubert et al., 2001)

$$\Delta T_H = a_f \frac{Hd^2}{k_m}, \tag{9}$$

where H is the volumetric heat production, d the thickness of the convective layer and k_m is the thermal conductivity. The factor

$$a_f = \frac{1}{3}\left[1 + \frac{R_{con}}{R_{con}+d} + \left(\frac{R_{con}}{R_{con}+d}\right)^2\right] \tag{10}$$

is the correction due to the spherical geometry (Deschamps et al., 2012), where R_{con} is the radial distance from the centre of Io to the bottom of the convective layer.

To estimate the lateral heat flow and to approximate the geotherm throughout the convective layer we need to know the Rayleigh-Roberts number (Roberts, 1967). The Rayleigh-Roberts number is a variant of the Rayleigh number describing the ratio between convection driving and convection inhibiting forces (Schubert et al., 2001) for a volumetric heated system and is given by

$$Ra_H = \frac{a_f \rho_m g \alpha H d^5}{k_m \eta_{con} \kappa}, \tag{11}$$

where ρ_m is the reference mantle density, κ is the thermal diffusivity, η_{con} the mantle convection viscosity, α the thermal expansion coefficient, and g the acceleration of gravity. Since we only consider direct effects of the tidal dissipation pattern on the temperature distribution, we assume that these mantle properties do not change with depth throughout the convective system. The influence of a radially non-homogeneous heating on the temperature profile of a convective system has been investigated for a two-layered spherically symmetric heating pattern (Vilella and Kaminski, 2017). However, to our knowledge no scaling laws are available that can deal with complex radially varying heating distributions, as for Io. That is why we merge the three dimensional volumetric heating patterns $H(r,\theta,\phi)$ obtained in Section 2 into a two-dimensional pattern

$$Q'(\theta,\phi) = \int_{R_{con}}^{R_{con}+d} H(r,\theta,\phi)\mathrm{d}r, \tag{12}$$

where d is the thickness of the simultaneously internally heated and convective layer. Note that $Q'(\theta,\phi)$ obtained from Eq. (12) is not Io's

actual heat flux $Q(\theta,\phi)$. $Q'(\theta,\phi)$ is the pattern of the heat production rate per unit area, or, in other words, a projection of the produced three-dimensional volumetric heat production onto Io's surface. In the following the blurring model, which estimates the actual heat flux pattern $Q(\theta,\phi)$ taking into account lateral flow due to convection, is explained.

3.2. Lateral heat flow due to convection

The heat flow in a convective medium is not only in radial direction but also in lateral direction. This convective heat flow in lateral direction results in a lateral smoothing of the spatial varying heating pattern. Blurring can be described as a weakening of higher degrees of the computed power spectrum of the dissipation pattern, thus it acts as a low-pass filter. The heat production rate per unit area is decomposed into spherical harmonics:

$$Q'(\theta,\phi) = \overline{Q}' + \sum_{n=1}^{n_{max}} \sum_{m=0}^{n} \overline{P}_{nm}(\cos\theta)(C_{nm}\cos(m\phi) + S_{nm}\sin(m\phi)). \tag{13}$$

$\overline{P}_{nm}$ is the fully normalized associated Legendre function of degree n and order m and $\overline{Q}'$ the mean global heat flux. The actual total heat flux function is derived by

$$Q(\theta,\phi) = \overline{Q} + \sum_{n=1}^{n_{max}} B(n) \sum_{m=0}^{n} \overline{P}_{nm}(\cos\theta)(C_{nm}\cos(m\phi) + S_{nm}\sin(m\phi)), \tag{14}$$

with

$$\overline{Q}' = \overline{Q}. \tag{15}$$

The blurring is achieved through a filter $B(n)$, i.e. the blurring factor, which is given by

$$B(n) = C\overline{Ra}_H^{-\beta}\frac{R\pi}{nd}. \tag{16}$$

According to Tackley (2001), C is a constant and β is equal to 1/4 for the analytically investigated homogeneous case. However, for a boundary-focused heating profile, characteristic for Io's asthenosphere (Tackley et al., 2001), β changes its value as shown numerically by Tackley (2001). The effectiveness of the blurring is approximated using the globally averaged Rayleigh-Roberts number

$$\overline{Ra}_H = \frac{a_f \rho_m g \alpha \overline{f}_{cc}\,\overline{Q} d^4}{k_m \overline{\eta}_{con}\kappa}, \tag{17}$$

which is derived from Eq. (11), but here given as a function of the globally averaged convective-conductive heat flux $\overline{f}_{cc}\,\overline{Q}$ and the reference mantle viscosity $\overline{\eta}_{con}$. Because we do not consider any radial fluctuation of the blurring strength, we replace the volumetric heat H with Q/d. To fulfil the conservation of energy, the globally averaged heat flux ($n = 0$) needs to remain the same (see Eq. (15)). Consequently, $B(n = 0)$ is set equal to 1. As none of the higher degree signals should be increased by the blurring, $B(n > 0)$ is forced to be 1 if resulting in a value larger than 1. From Eqs. (13) and (16) it becomes obvious that a large Rayleigh-Roberts number $\overline{Ra}_H$ as well as a large convective layer thickness d cause strong blurring of the tidal dissipation signal.

Also the magmatic heat output driven by melt $Q'_{mag}(\theta,\phi)$, calculated in Section 3.4, needs to be blurred in order to approximate the amount of heat neighbouring regions can feed a magma reservoir due to convective motion. This allows the surface heat output by melt $Q'_{mag}(\theta,\phi)$ to regionally exceed the tidal heat production directly produced below a specific area, which is usually the case for magmatic systems.

3.3. Thermal profile of Io's internally heated mantle

Next, we compute the maximum mantle temperature at the bottom of the thermal boundary layer and corresponding properties of Io's thermal profile using the parameters determined in Section 3.1. For that, only the convective-conductive part of the heat flux $Q_{cc}(\theta,\phi)$ (Eq. (8)) is considered. In contrast to the approximation of the blurring where we considered a global average Rayleigh-Roberts number (Eq. (17)) because of the global filtering approach (Eq. (14)), the Rayleigh-Roberts number $Ra_H(\theta,\phi)$ is treated as a spatial-dependent property of the interior here.

The relation between the convective-conductive heat flux and magmatic heat flux changes locally, since we assume that the intensity of the magmatic heat flux depends on the amount of melt. The melt distribution is initially unknown, as it depends on the initially unknown local mantle temperature and initially unknown distribution of $Q_{cc,final}(\theta,\phi)$. That is why we take the global average convective-conductive heat flux $Q_{cc,i=1} = \overline{f}_{cc}\,Q(\theta,\phi)$ as an a-priori value in the first iteration step $i = 1$. Each further iteration step $Q_{cc,i}(\theta,\phi)$ is updated (see Fig. 1), until the final distribution of the heat flux variation $Q_{cc,final}(\theta,\phi)$ is found. Thereby, the local heat flux fraction $f_{cc,i}(\theta,\phi)$ between the local heat flux $Q(\theta,\phi)$ and the convective-conductive heat flux $Q_{cc,i}(\theta,\phi)$ is allowed to change. However, we force the globally averaged convective-conductive heat flux $\overline{Q}_{cc}$ and consequently the heat flux fraction $\overline{f}_{cc}$ given in Eq. (8) to remain constant for each iteration step.

We substitute H/d with the convective-conductive heat flux $Q_{cc,i}(\theta,\phi)$ in Eqs. (11) and (9). The Rayleigh-Roberts number distribution for each iteration step i is therefore given by

$$Ra_{H,i}(\theta,\phi) = \frac{a_f \rho_m g \alpha Q_{cc,i}(\theta,\phi) d^4}{k_m \eta_{con}(\theta,\phi)\kappa}, \tag{18}$$

and the distribution of the a-priori temperature jump across the convective layer is given by

$$\Delta T_{H,i}(\theta,\phi) = a_f \frac{Q_{cc,i}(\theta,\phi) d}{k_m}. \tag{19}$$

We use the scaling law introduced by Vilella and Kaminski (2017) to approximate the temperature at the top of up-streaming vents just below the thermal boundary layer, i.e. the maximum mantle temperature (Vilella and Kaminski, 2017). We follow their approach for two reasons: 1) The scaling is based on an analytical description allowing to consider a wide range of the Rayleigh-Roberts numbers. 2) Other scaling laws for volumetric heating schemes (e.g. Parmentier et al., 1994) investigate the mean mantle temperature. Using these kind of scaling laws, we would underestimate the melt fraction. As described in Vilella and Kaminski (2017) this maximum mantle temperature arising in hot up-streams is not omnipresent in a convective mantle. Thus, applying the resulting temperature and corresponding melt fraction globally, would result in an over-estimation of the presence of melt. However, the fraction between hot up-streams and cold down-streams is implicitly included in the variable $\overline{f}_{cc}$, which we use for the estimation of the heat flux transported by melt in Section 3.4. As the variable $\overline{f}_{cc}$ comprises a large set of poorly known parameters it is investigated for a wide range of possible values. Thus, an explicit knowledge of the surface fraction is not required, as long as we assume that the up-streams are uniformly distributed. A schematic temperature profile with all the important parameters introduced in the following is shown in Fig. 2.

The maximum temperature jump $\Delta T_{top,i}(\theta,\phi)$ across the thermal boundary layer is determined by

$$\Delta T_{top,i}(\theta,\phi) = \frac{1}{2}\Delta T_{H,i}(\theta,\phi)\left(\frac{Ra_{H,crit}}{Ra_{H,i}(\theta,\phi)}\right)^{1/4}, \tag{20}$$

following Vilella and Kaminski (2017). In contrast to Eq. (18) in Vilella and Kaminski (2017) the spherical symmetric correction factor a_f is not included in Eq. (20), as the correction is already included in $\Delta T_{H,i}$ (Eq.

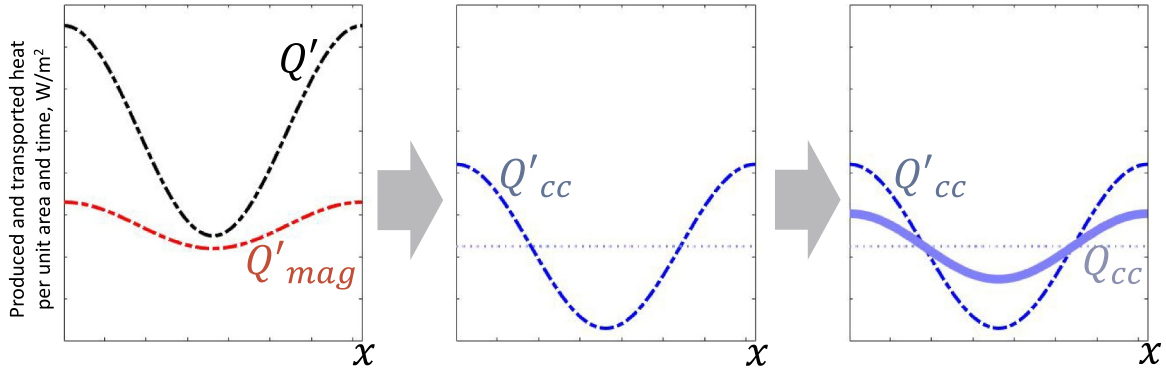

Fig. 3. Schematic graph of a heat production and heat transport profile along an arbitrary profile x (one wavelength only). Out of the total produced heat per unit area and unit time Q' (black dashed line) and the magmatic heat output Q'_{mag} (red dashed line) we derive the amount of remaining heat that needs to be transported by mantle convection. We get $Q'_{cc} = Q' - Q'_{mag}$ (blue dashed line). For Q'_{cc} the lateral flow due to convection is not considered. Therefore, Q'_{cc} is blurred to account for lateral flow and we get Q_{cc} (blue solid line). Regions with $Q'_{cc} > Q_{cc}$ have a negative lateral net heat flow. Regions with $Q'_{cc} < Q_{cc}$ have a positive lateral net heat flow. The average convective heat flow $\overline{Q}_{cc}$ (thin dotted blue line) remains the same for Q'_{cc} and Q_{cc}. (For interpretation of the references to colour in this figure legend, the reader is referred to the web version of this article.)

(19)). The critical Rayleigh-Roberts number $Ra_{H,crit}$ provides a threshold value that determines whether the system is convective or conductive. The maximum mantle temperature at the corresponding latitude and longitude is a function of the maximum temperature jump across the thermal boundary layer $\Delta T_{top,i}$ and can be approximated by (Grasset and Parmentier, 1998; Tosi et al., 2017)

$$T_{m,i}(\theta,\phi) = \sqrt{\Delta T_{top,i}(\theta,\phi)\frac{E_a}{2.9R_{gas}}}, \tag{21}$$

with the activation energy E_a and the gas constant R_{gas}.

Substituting Eqs. (18) and (19) into Eq. (21) and further simplification results in a new expression for the maximum mantle temperature

$$T_{m,i}(\theta,\phi) = \gamma_0 (a_f Q_{cc,i}(\theta,\phi))^{\frac{3}{8}} \eta_{con}(\theta,\phi)^{\frac{1}{8}}, \tag{22}$$

with

$$\gamma_0 = \sqrt{\frac{E_a}{5.8R_{gas}}}\left(\frac{\kappa Ra_{H,crit}}{\rho_m g \alpha k_m^3}\right)^{\frac{1}{8}}. \tag{23}$$

From Eq. (22) it can be seen that the maximum mantle temperature increases with increasing viscosity and increasing magmatic heat output.

Note that $\eta_{con}(\theta,\phi)$ is not constant as it depends on the mantle temperature distribution $T_m(\theta,\phi)$. Despite this being a minor effect, we developed a procedure correcting for it using the Lambert relation. We describe the full procedure in Appendix A.

3.4. Magmatic heat transport by melt and iterative procedure

We assume that the amount of heat transported by magma in a certain region depends on the local melt fraction. To calculate the latter, we follow Katz et al. (2003) considering an anhydrous solidus of a peridotitic lherzolite, which can be found in the Earth's mantle. The parametrization for the melt fraction is a function of pressure and temperature and serves as a good approximation of the ultra-mafic material, which is present at some of Io's volcanoes (Davies et al., 2010). Note, however, that sulphur is an abundant material on Io's surface and plays an important role in Io's volcanic activity. The melting temperature reducing effect of sulphur is not included in this study, since the presence and influence of sulphur in Io's deep layers are not well known.

The melt fraction is given as a fractional distance between solidus and liquidus (Hirschmann, 2000)

$$\overline{\Pi_i}(\theta,\phi) = \frac{T_{m,i}(\theta,\phi) - T_{sol}(P)}{T_{liq}(P) - T_{sol}(P)}, \tag{24}$$

where $T_{sol}(P)$ and $T_{liq}(P)$ are polynomial functions of the pressure P (Katz et al., 2003). Note that the above version of the melt parametrization results in small but increasing inaccuracies with increasing melt fractions. Furthermore, we ignore any spatial variation of the crustal thickness (Eq. (31)) as well as the thickness of the thermal boundary layer, and approximate the maximum melt fraction at the depth of the initial crustal thickness of the rheological model (Section 2). From Eq. (24) we calculate the globally averaged maximum melt fraction $\overline{\Pi_i}$ in up-rising plumes.

Parameters that determine how much melt is transported per surface fraction are difficult to predict for Io. We assume that the melt transport efficiency is proportional to the melt fraction just below the thermal boundary layer, and that the melt-containing up-streams are not omnipresent but equally distributed. Thus, we determine the global heat transport efficiency

$$\overline{\varphi}_{melt,i} = \frac{\overline{Q}_{mag}}{\overline{\Pi_i}}, \tag{25}$$

using the average global magmatic heat flux $\overline{Q}_{mag} = (1 - \overline{f}_{cc})\overline{Q}$ and the globally averaged melt fraction $\overline{\Pi_i}$. Note again, that $\overline{Q}$ is an observational constraint and the variable $\overline{f}_{cc}$ is constant throughout the iterations. The factor $\overline{\varphi}_{melt,i}$ determines a heat flux per melt fraction. It combines several heat pipe parameters, such as the fraction of hot up-streams within a certain area, the latent heat, the buoyancy or corresponding velocity and the density of melt as used by Bierson and Nimmo (2016), Elder (2015), and Moore (2001). Next, we solve for the magmatic heat output per unit area

$$Q'_{mag,i}(\theta,\phi) = \overline{\varphi}_{melt,i}\overline{\Pi_i}(\theta,\phi). \tag{26}$$

$Q'_{mag,i}(\theta,\phi)$ is considered as a negative heat source per unit area, i.e. the opposite sign as the produced heat $Q'(\theta,\phi)$. We apply the blurring filter (Eq. (16)) resulting in $Q_{mag,i}(\theta,\phi)$ and obtain the new convective-conductive heat flux:

$$Q_{cc,i+1}(\theta,\phi) = Q(\theta,\phi) - Q_{mag,i}(\theta,\phi). \tag{27}$$

Due to the linear behaviour of the blurring filter it is also possible to derive $Q_{cc,i+1}(\theta,\phi)$ given in Eq. (27) in a different way (Fig. 3).

We enter the result of Eq. (27) into Eq. (22) and recalculate Eqs. (22)–(26) until convergence is found. This way an equilibrium between convective-conductive and magmatic heat flux for each co-latitude and longitude is found for a specific set of input parameters. The obtained equilibrium considers the initial heat production, the convective

manner of the asthenosphere and mantle, the temperature-dependence of melt occurrence, and heat transport by melt. Once convergence is found ($Q_{cc,i-1} \approx Q_{cc,i} = Q_{cc,final}$) we obtain the posteriori lateral pattern of $T_m(\theta,\phi)$, $Q'_{mag}(\theta,\phi)$, $Q_{cc}(\theta,\phi)$ and the lateral varying melt distribution $\Pi(\theta,\phi)$ (see Fig. 1).

3.5. Lateral thickness variations of the thermal boundary and crust

In the last step, we check whether our thermal models result in crustal thicknesses in agreement with the rheological structure given in Section 2.3. For that, the final heat flux distribution $Q_{cc}(\theta,\phi)$ and the final maximum mantle temperature $T_m(\theta,\phi)$ are taken into account.

The thickness of the boundary layer is calculated according to Vilella and Kaminski (2017):

$$\delta_{top}(\theta,\phi)/d = \left(\frac{Ra_{H,crit}}{Ra_H(\theta,\phi)}\right)^{1/4}. \tag{28}$$

From Eq. (21) we get the maximum temperature below the lid

$$T_{lid}(\theta,\phi) = T_m(\theta,\phi) - \Delta T_{top}(\theta,\phi). \tag{29}$$

We calculate the thickness of the conductive stagnant lid

$$\delta_{lid}(\theta,\phi) = k_{lid}\frac{T_{lid}(\theta,\phi) - T_s}{Q_{cc,i}(\theta,\phi)}, \tag{30}$$

where k_{lid} is the thermal conductivity of the stagnant lid and T_s is the surface temperature. Both parameters are assumed to be spatially uniform. We neglect any heat production in the conductive lid. Further, we assume that the conductive heat flux in the stagnant lid is equal to the convective heat flux in the mantle. Finally, we obtain the conductive crustal thickness (Fig. 2), adding the thickness of the thermal boundary layer and the thickness of the stagnant lid:

$$\delta_{crust}(\theta,\phi) = \delta_{lid}(\theta,\phi) + \delta_{top}(\theta,\phi). \tag{31}$$

Note the minor discrepancy between the thermal and the visco-elastic model. For the thermal model the thermal boundary layer belongs to the heated asthenosphere, however, its visco-elastic characteristics are more in agreement with the crust. However, this discrepancy has no effect on our results and conclusions because the evolving thickness of the thermal boundary layer is very small for most of the investigated mantle viscosities.

3.6. Thermal properties of Io models

In this section we discuss the thermal properties of the two end-member cases that have already been introduced in Section 2. For Model A, we allow only the asthenosphere to be convective because all of the tidal heating will occur in the asthenosphere (defined in Table 3). We treat the asthenosphere-deep mantle boundary as a non-permeable layer, allowing no exchange of material and neglect the heat flux from the core and the deep mantle. A fully convective mantle including the deep mantle and the asthenosphere is assumed for Model B. As presented in Table 3 both the deep mantle and the asthenosphere are heated by tides and therefore need to lose heat efficiently. Accordingly, the thickness of the convective layer d and the geometrical correction for the spherical geometry a_f for Model B are different from Model A.

For simplicity, we assume that the mantle properties such as the viscosity η_{con}, the density ρ_m, the thermal expansivity α, the conductivity k_m and the diffusivity κ (all given in Table 2) are constant throughout the convective system. We also consider the mantle viscosity η_{con} for Model B to be radially constant, but we use different Maxwell viscosities η_{diss} for the deep mantle and the asthenosphere (Table 3). For the stagnant lid, which is assumed to be present for Io (Moore, 2003), the critical Rayleigh-Roberts number is 2772 (Roberts, 1967). The respective proportionality constants C and β quantifying the strength of the blurring are taken for a boundary-focused heating profile from Tackley (2001) (both given in Table 2). The average gravitational acceleration g is calculated at the top of the convective system based on the density profile given in Section 2. The surface temperature T_s is set to 100 K as done in Moore (2003) and the thermal conductivity of the lid k_{lid} is the same as for the mantle.

4. Results

In this section we present the volumetric heat distribution of our benchmarked finite element models. Further, we follow Sections 3.3 and 3.4 and present the spatial temperature, melt, and heat flux patterns for selected sets of interior parameters. This is followed by a parameter study, investigating the strength of the tidally-induced effect on Io's interior for a wide range of parameters.

4.1. Tidal dissipation pattern of the finite element model

We set up the numerical model as described in Section 2. All model specific adjustments and a benchmark showing that the accuracies of the numerical results are sufficient for further use can be found in Appendix B. The resulting spatial patterns of heat production $H(r,\phi,\theta)$ for both models, averaged over one orbit are given in Fig. 4.

For Model A, strong heating is present at the lid-asthenosphere-boundary and at the asthenosphere-deep-mantle-boundary. This is because strong lateral deformation is present within the viscous asthenosphere causing friction at the boundaries. These deformations are smaller towards high latitudes. In the polar cut, large variations between the polar areas at 90° N and 90° S and the equatorial areas are seen. The rheological structure chosen for Model B results in a more evenly distributed volumetric heat production.

The differences between Model A and Model B become also obvious in the two-dimensional pattern of the heat production rate per unit area $Q'(\phi,\theta)$ (Fig. 5) obtained after the radial integration of the produced heat. Both rheological structures have a similar average heat flux (Table B.1) but result in different dissipation patterns. For Model A 30° North and South of the sub-Jovian point the maximum areal heat production is approximately 3.6 W m^{-2} and no tidal heat is produced at the poles. For Model B the heat generation is more evenly distributed. The patterns in panels a and b in Fig. 5 are qualitatively compatible to Figs. 2b and 3c in Ross et al. (1990) for which slightly different rheological structures were used.

4.2. Spatial patterns of temperature, magmatic heat output, melt fraction and crustal thickness

In this section we calculate the temperature, magmatic heat flux, melt fraction and crustal thickness for a set of main input parameters, which are the heat flux fraction $\overline{f}_{cc}$ and the reference mantle viscosity $\overline{\eta}_{con}$. The sets only produce one out of many possible outcomes for Model A and Model B and are chosen in a way that the input values are realistic to describe Io's interior and on the other hand result in model outputs close to our initial rheological model. For the filter we chose $n_{max} = 10$ (Eq. (14)). This is sufficient to describe the modelled tidal dissipation pattern, which, apart from minor numeric-induced artefacts, only contains components of $n \leq 4$ (Beuthe, 2013). Next, we iterate Eqs. (22)–(26). We only consider solutions that fulfil the convergence criteria of $(Q_{cc,i-1} - Q_{cc,i}) < 10^{-3}$ W m^{-2} for each single co-latitude and longitude within 400 iterations. However, for most of the models this is achieved in 20–30 iterations. Testing for different starting values and step sizes indicates that the obtained results are stable.

The two different sets of reference mantle viscosity and heat flux fraction and major resulting interior properties are presented in Table 4. For Model A and Model B the chosen parameter sets result in a globally averaged maximum mantle temperature $\overline{T}_m$ close to 1513 K. This temperature corresponds to the solidus temperature at a depth of 230 km (Section 3.4) implying a 200 km thick partially molten layer.

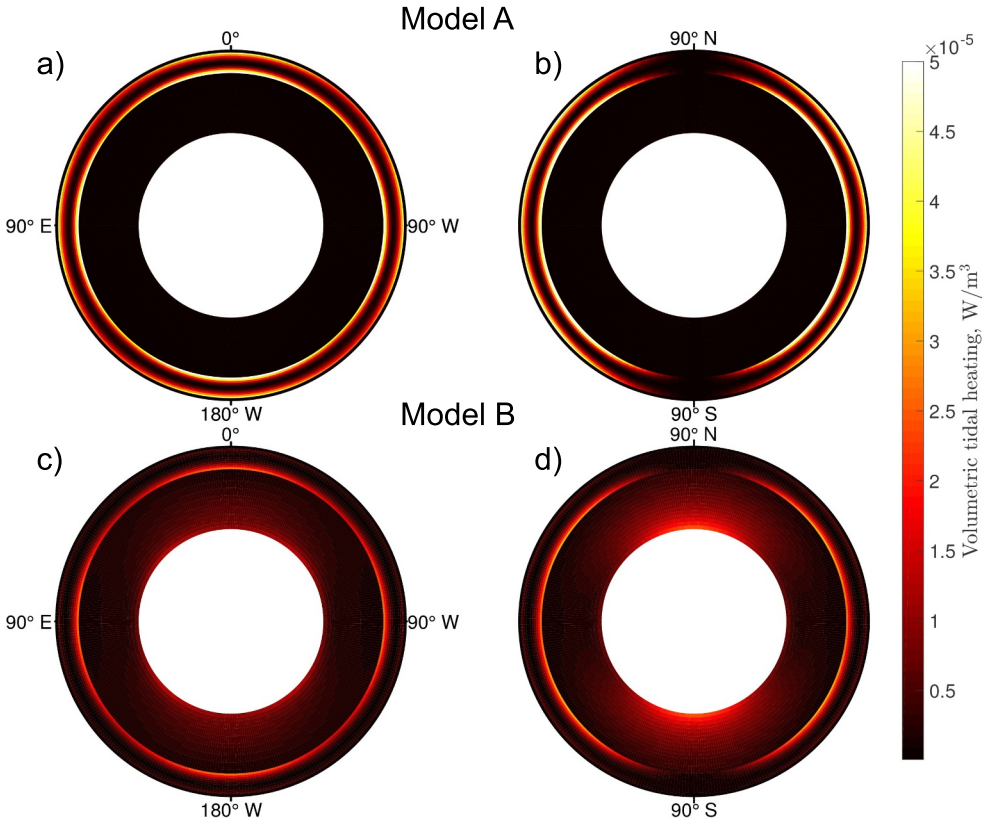

Fig. 4. Volumetric dissipation in Io's mantle and asthenosphere Model A and Model B. a) and c) Cross-sections along Io's equator plane for Model A and Model B, respectively. b) and d) Cross-sections along the plane of the North and South pole, and Io's sub-Jovian point.

However, only for Model B we achieve an average crustal thickness of approximately 30 km as provided in the initial rheological model (Table 2). Because of the difference in the thickness of the convective layer d no solution can be found for Model A for the chosen parameter set of Model B and vice versa. This will be discussed in more detail in Section 4.3.

We visualize the spatial distribution of the maximum mantle temperature $T_m(\theta,\phi)$, the magmatic heat output $Q'_{mag}(\theta,\phi)$, the distribution of the melt fraction $\Pi(\theta,\phi)$ and the crustal thickness δ_{crust} for both model specific parameter sets of Model A and B in Fig. 6. The mantle temperature patterns of Model A and Model B (Fig. 6a and b) follow the pattern of the areal heat production (Fig. 5). However, all degree 4 components are significantly suppressed due to the lateral convection as simulated by the blurring filter. Note again that the presented temperature distribution gives maximal possible values of the mantle temperature at the bottom of the thermal boundary layer and is only valid in case a hot up-streaming plume is present below this location. In addition, temperature buffering near the solidus due to latent heat is not included (Ross et al., 1990). The resulting melt fractions also

Table 4
Parameter sets of $\overline{f}_{cc}$ and $\overline{\eta}_{con}$ for Model A and Model B, which result in similar globally averaged maximum mantle temperature $\overline{T}_m$.

Model	$\overline{f}_{cc}$	$\overline{\eta}_{con}$	$\overline{\delta}_{crust}$	$\overline{T}_m$	max(T_m)-min(T_m)
A	0.18	$4.6{\cdot}10^{14}$ Pa s	12.7 km	1514.0 K	98.1 K
B	0.0815	$1.34{\cdot}10^{16}$ Pa s	29.4 km	1514.5 K	18.9 K

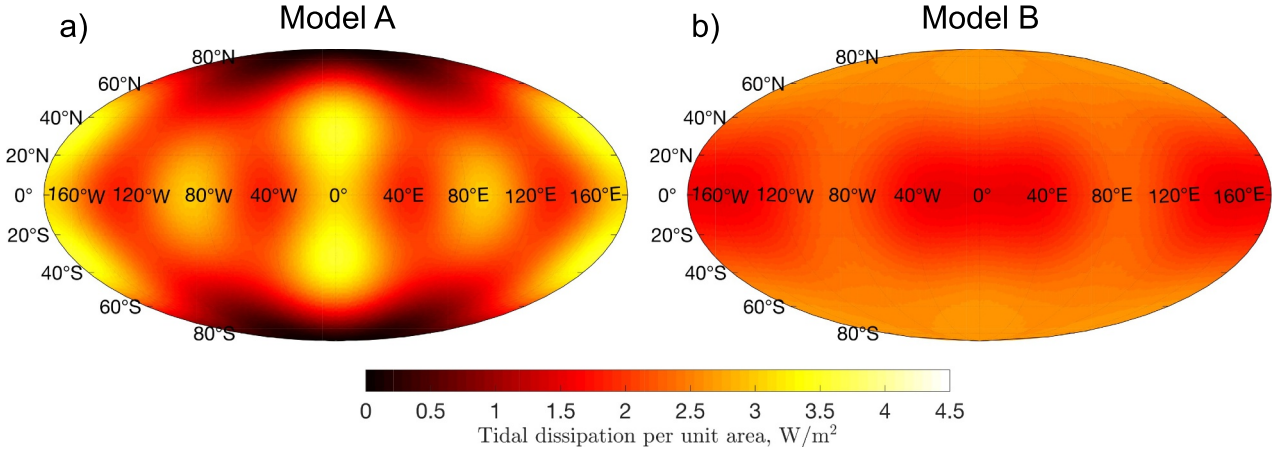

Fig. 5. Produced heat per unit area projected onto Io's surface (Mollweide projection) for Model A (a) and Model B (b).

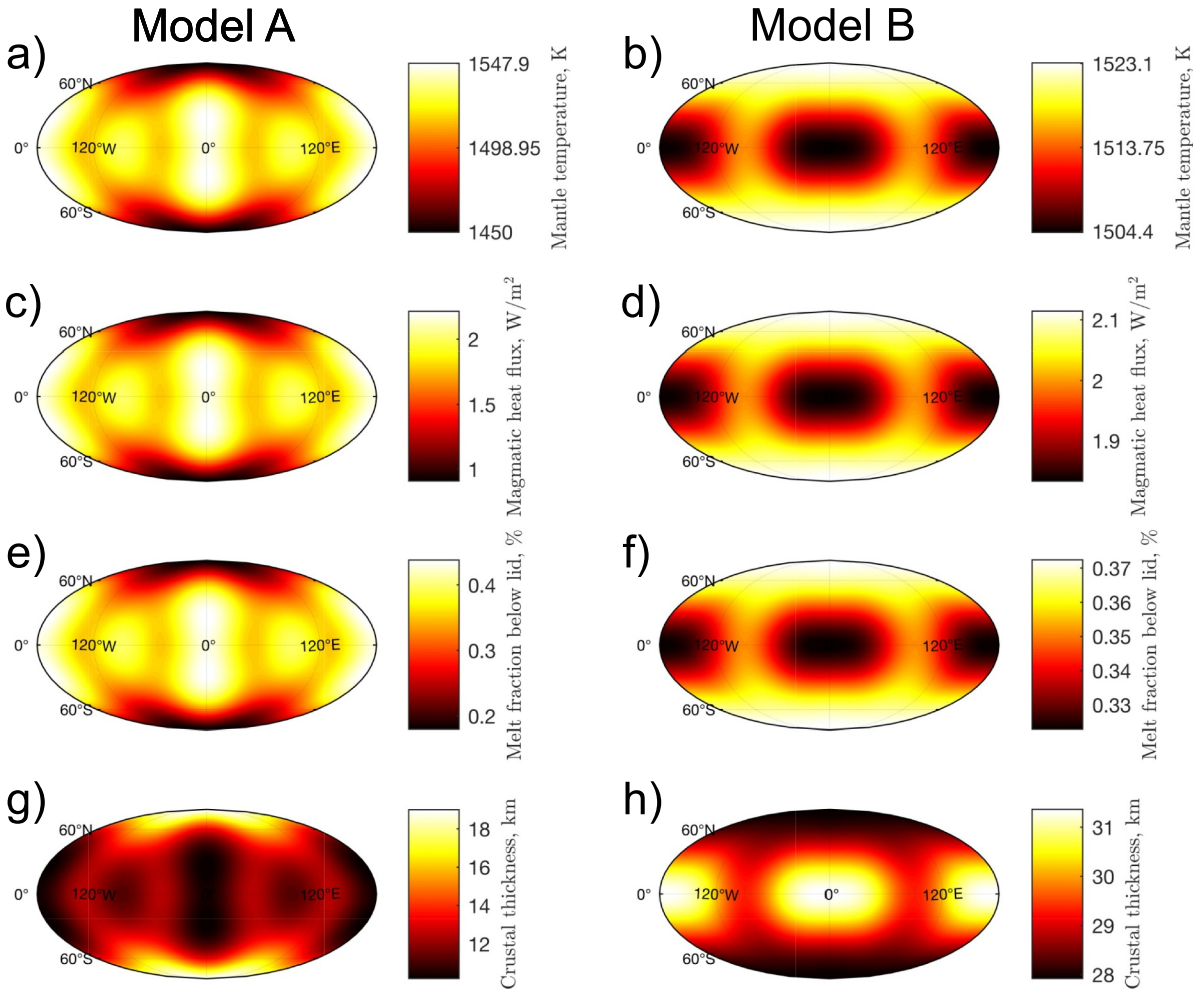

Fig. 6. Spatial pattern of maximum mantle temperature (a and b), magmatic heat output (c and d), melt fraction (e and f), and crustal thickness (g and h) for Model A and Model B, respectively.

represent maximum values (Fig. 6e and f). The average melt fractions are consequently much lower.

The magmatic heat output is assumed to be proportional to the volcanic activity level. Consequently, the resulting magmatic heat output maps can be used to indicate the expected eruption intensity and frequency for Io. For Model B the volcanic activity due to any tidally induced lateral varying thermal differences fluctuates about 7% around its average value. This fluctuation might be too small to be detected through long-term observations of Io's volcanic activity pattern. For the chosen parameter set of Model A a fluctuation of around 37% can be expected. The crustal thickness maps (Fig. 6g and h) show converted patterns of the temperature distribution. Note that processes such as volcanic re-surfacing, near-surface intrusions, and the change in effectiveness of melt advection with changing crustal thickness are neglected (O'Reilly and Davies, 1981; Stevenson and McNamara, 1988).

4.3. Influence of interior parameters

In the following, we derive the average maximum mantle temperature $\overline{T}_m$, the maximum temperature variation (peak-to-peak), the maximum difference of the normalized magmatic heat output (max (Q'_{mag})-min(Q'_{mag}))/$\overline{Q}_{mag}$, and the average crustal thickness for a wide range of $\overline{\eta}_{con}$ and $\overline{f}_{cc}$ according to Table 2. We use the normalized value here for the magmatic heat output, as $\overline{Q}_{mag}$ changes with $\overline{f}_{cc}$. By normalizing the peak-to-peak values with $\overline{Q}_{mag}$, the relative differences in the strength of the magmatic heat output, and hence the relative difference of the volcanic activity level, become comparable. The results for Model A and Model B are presented in Fig. 7a–h. The Rayleigh-Roberts number, which quantifies the vigor of the convective flow and thus the strength of the blurring (Eq. (16)), is presented in Appendix C.

Although we test all combinations of $\overline{f}_{cc}$ and $\overline{\eta}_{con}$, solutions can only be found for the coloured regions. A reason for this is that the maximum mantle temperatures need to be between the solidus and liquidus. In case no melt is present no heat can be transported by melt. Thus, no solution can be found for $\overline{f}_{cc} < 1$. Furthermore, melt fractions larger than 1 at any location are not allowed. Due to these boundary conditions valid solutions are found to be in parabolic-shaped regions running from high $\overline{f}_{cc}$ and low $\overline{\eta}_{con}$ values to low $\overline{f}_{cc}$ and high $\overline{\eta}_{con}$ values. Within these regions the highest average maximum temperatures are obtained for high $\overline{f}_{cc}$ values and high reference viscosities $\overline{\eta}_{con}$ (subfigures a and b of Fig. 7). A high viscosity suppresses vigorous mantle convection leading to higher mantle temperatures. A mantle in thermal equilibrium with a high fraction of magmatic heat transport (low $\overline{f}_{cc}$ value) would be cooler than a mantle with the same reference mantle viscosity but a low fraction of magmatic heat transport (high $\overline{f}_{cc}$ value).

In contrast to Model B, we cannot find solutions for any parameter sets with $\overline{f}_{cc} < 0.17$ for Model A. This can be explained as follows: For parameter sets resulting in a low average maximum mantle temperature but large temperature differences, the temperature does not remain above the solidus for each location. Consequently, only some regions sustain melt. However, in the case where we force the model to yield a high fraction of global magmatic heat output (low $\overline{f}_{cc}$ value), the regions

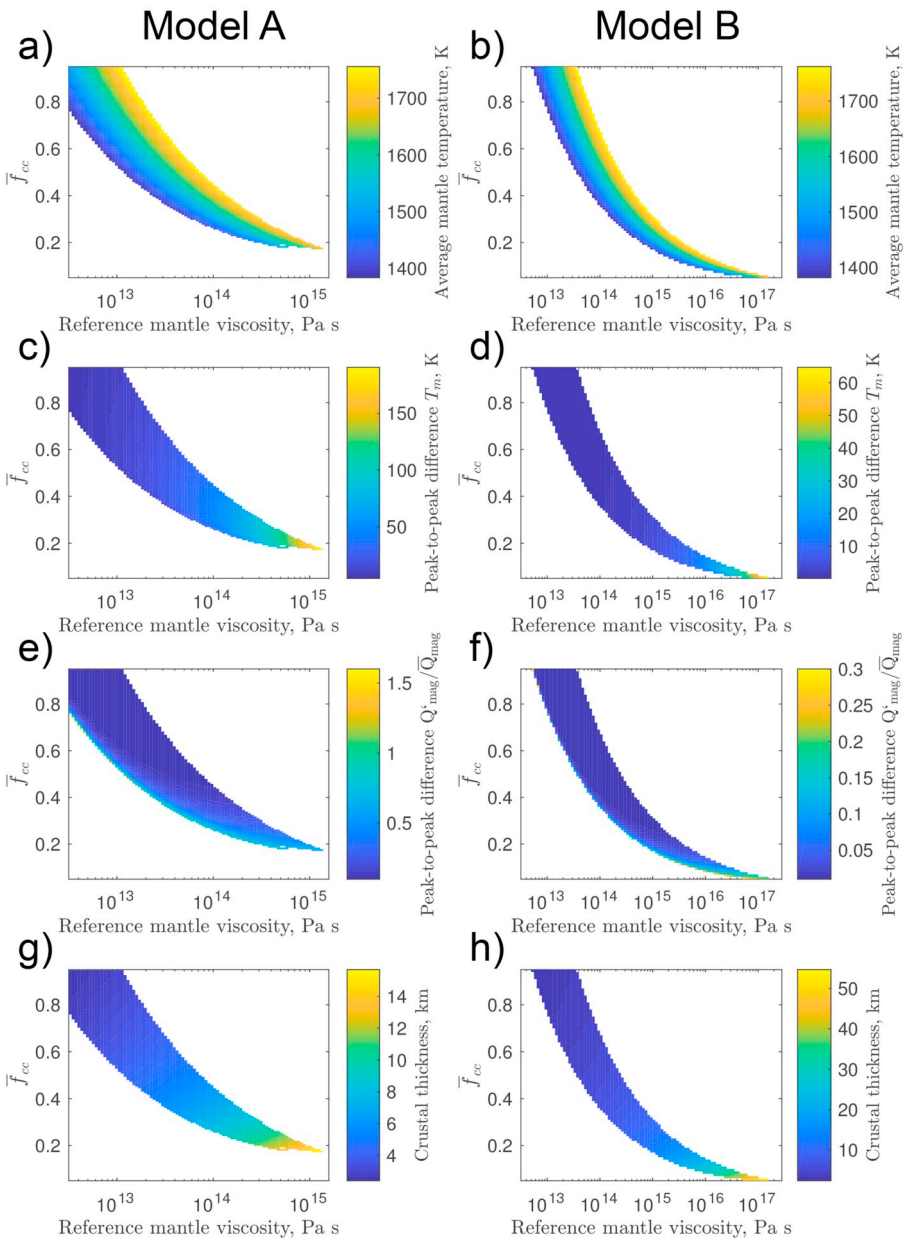

Fig. 7. The figure shows average maximum mantle temperature (a and b), peak-to-peak temperature difference (c and d), normalized peak-to-peak magmatic heat output per unit area (e and f), and average crustal thickness (g–h) for Model A and Model B as a function of the mantle viscosity $\overline{\eta}_{con}$ and $\overline{f}_{cc}$. $\overline{f}_{cc}$ quantifies the dominant heat transport mechanism, with small values representing models with a magma-dominating heat transport, and values close to 1 representing models with a convection-dominating heat transport. Note the different scales for the reference viscosities.

that sustain a mantle temperature above the solidus need to maintain a high magmatic heat output per unit area $Q'_{mag}(\theta,\phi)$. This magmatic heat output per unit area $Q'_{mag}(\theta,\phi)$ can be theoretically larger than the heat $Q'(\theta,\phi)$ produced directly underneath this location, but only up to the extent to which convection is able to provide the remaining heat from the neighbouring regions. Viewed analytically, $Q_{cc,i}(\theta,\phi)$ needs to be positive (Eq. (27)) in order for Eq. (22) to result in a non-imaginary value and allow for convergence. This implies that for a very strong initial dissipation pattern with very high fluctuations and a thin convective layer, such as for Model A, a low mantle viscosity and a convective-conductive heat flux fraction larger than 0.17 are necessary.

Not all of the successfully converged parameter sets (Fig. 7) necessarily result in realistic interior models. Parameter sets resulting in high average mantle temperatures causing an average melt fractions above 40% are inconsistent with model assumptions: 1) The melt fraction computation based on Katz et al. (2003) is only valid for low melt fractions. 2) The melt transport model is based on the assumptions that melt flows through pores in a solid matrix, which is only valid for melt fractions below 30% (Moore, 2001). However, the obtained melt fractions estimates give maximum values and occur only locally. Hot up-streams are not omnipresent and Io's sub-adiabatic geotherm and increasing pressures prevent melt production for deeper layers. Thus, even we do not favour these sets, we decide not to eliminate them from our results. Also parameter sets resulting in an average crustal thickness below 8 km are not favoured (Fig. 7g), but are included in the graphs for the sake of completeness.

Io's melt fraction obtained from observations is still under discussion (Khurana et al., 2011; Roth et al., 2017) and cannot be used to constrain the parameter space. Note that the parameter γ_0 (Eq. (23)) contains a collection of parameters determining the mantle convection. Some of these parameters, such as the activation energy E_a, the thermal conductivity k_m, and the critical Rayleigh-Roberts number are not

exactly known. For a smaller γ_0 the parabolic line of Fig. 7 would be shifted to larger viscosities. Thus, the reference viscosity would need to be larger to reach the comparable average maximum mantle temperatures and peak-to-peak differences. The opposite is the case for a larger γ_0.

The maximum temperature fluctuations (peak-to-peak) for Model A shown in Fig. 7c are more than one order of magnitude larger than for sets with the same reference mantle viscosities of Model B. For Model A peak-to-peak maximum mantle temperature differences between 5 K ($\bar{f}_{cc} = 0.95$ and $\bar{\eta}_{con} = 10^{12}$ Pa s) and 190 K ($\bar{f}_{cc} = 0.17$ and $\bar{\eta}_{con} = 1.3{\cdot}10^{15}$ Pa s) are achieved. Differences < 1 K ($\bar{f}_{cc} = 0.95$ and $\bar{\eta}_{con} = 10^{12}$ Pa s) up to 65 K ($\bar{f}_{cc} = 0.05$ and $\bar{\eta}_{con} = 1.4{\cdot}10^{17}$ Pa s) are found for Model B.

The average crustal thickness, shown in Fig. 7g and h, is affected by the dominating heat transport mechanism. It decreases with decreasing $\bar{\eta}_{con}$ and increasing $\bar{f}_{cc}$. For Model B we find a crustal thickness that is equal to the starting assumption of 30 km for $\bar{f}_{cc}$ in the range 0.075–0.09. Due to the lack of convergence for specific parameter sets, discussed above, we cannot obtain a crustal thickness of 30 km for Model A. However, reasonable values within the lower range of the observational constraints for Io's crustal thickness are achieved. Large spatial fluctuations of the magmatic heat output as shown in Fig. 7e and f arise for low average maximum mantle temperatures and low global heat flux values. Although solutions can be found for low global heat flux values for Model B, peak-to-peak variations remain small (around 15% around the average value). Accurate and long-term observations of Io's active volcanic features will be necessary to detect this signal. For Model A a 91% fluctuation in volcanic activity around the average value is obtained, which is more easily detectable.

5. Discussion and conclusion

Io's exceptional position within the celestial bodies of the Solar System makes it a unique laboratory to investigate hot terrestrial bodies that undergo intense heat loss. In this study, we introduce a model that couples Io's non-uniform tidal dissipation with Io's main heat transport mechanisms, i.e. mantle convection and melt advection, to investigate the spatial effect of the heterogeneous heat production on Io's interior structure and surface heat flux. We investigate two spherically symmetric end-member models. For Model A only the asthenosphere is tidally heated and convective. For Model B, both Io's deep mantle and asthenosphere are tidally heated and convective. We compute the dissipation patterns using a finite element model based on Maxwell rheology and benchmark our results with semi-analytical models. For the thermal modelling, we combine 1) lateral convective flow simulated by reducing high-frequency signals (Tackley, 2001), 2) mantle convection for a volumetric heated regime using a steady-state scaling law by Vilella and Kaminski (2017) to compute the temperature within uprising plumes just below the thermal boundary layer, and 3) magmatic heat transport depending on the local melt fraction following Katz et al. (2003). The laterally varying heat transport mechanisms are iteratively adjusted until an equilibrium state of magmatic heat output and convective-conductive heat flux for each angular position is found.

One of the essential additions to former models is the coupling of convective and conductive heat transport with magmatic heat transport. This has been done previously by Elder (2015) for a one-dimensional heating structure using a different model approach, but is here incorporated for a three-dimensional heating pattern. In contrast to Bierson and Nimmo (2016) and Moore (2001), we assume that melt does not occur due to the necessity of heat transport but due to the temperature and pressure conditions favouring the occurrence of melt. Thus, we allow for a spatially varying mantle temperature pattern and a spatial varying depth of Io's melt containing layer. In addition, we include the spatial varying magmatic heat flux in the calculation of the temperature distribution.

The incorporation of melt migration allows for a wide range of mantle viscosities to result in realistic mantle temperatures. For Model A we acquire higher mantle viscosities for Io's asthenosphere than those obtained by Tackley (2001) and Tackley et al. (2001) for a purely convective heat transport. Thus, if Io sustains a large fraction of magmatic heat transport, no global magma ocean (Tyler et al., 2015) is required to explain Io's high heat output. Furthermore, the inclusion of magmatic heat transport also preserves the long-wavelength pattern of tidal dissipation. This is due to two reasons. First, the time scales of rising magma are much shorter than the convective time scales of solid material. Therefore, heat transport by magma facilitates a more radial heat flow direction than convection. Second, the addition of magmatic heat transport allows for a higher solid mantle viscosity due to the additional heat transport mechanism cooling the mantle. This allows Io's asthenosphere and mantle to sustain a thermal steady state with a less vigorous convection and less lateral smoothing of the initial tidal dissipation pattern. Further, the modelling approach is suitable to get a crustal thickness range in agreement with the literature (Turtle et al., 2007).

The results reveal that tidal dissipation within Io's interior can cause significant lateral variations in Io's interior structure. The strength of the tidally induced signal on Io's interior structure and surface depends to a large extent on the spatial variations of the initial tidal dissipation pattern $H(r, \phi, \theta)$. The variations are damped by a large thickness d of the convective system, a low reference convective mantle viscosity $\bar{\eta}_{con}$, and a high heat flux fraction $\bar{f}_{cc}$, i.e. a convection-dominating heat transport mechanism. Consequently, the two models result in very different peak-to-peak mantle temperature differences. For Model A differences between 5 K up to 190 K are achieved depending on the viscosity and dominating heat transport mechanism. Temperature differences of < 1 K and up to 65 K are found for Model B. Sets within the lower range of the $\bar{f}_{cc}$ fraction, corresponding to sets with significant peak-to-peak temperature differences, are favoured, since parameter sets with a high heat flux fraction $\bar{f}_{cc} > 0.4$ obtain very thin crustal thicknesses not in agreement with the observations. A better knowledge of $\bar{f}_{cc}$ is necessary to constrain Io's mantle viscosity and average mantle temperature (Fig. 7). Unfortunately, it is not possible to derive $\bar{f}_{cc}$ from Io's observed volcanic heat flow (Davies et al., 2015; de Kleer and de Pater, 2016; Veeder et al., 2015) and Io's poorly constrained continuous background heat flow. This is because the observed background heat flow could also arise from near-surface magmatic intrusions and former volcanic events (Stevenson and McNamara, 1988).

Investigating the modelled peak-to-peak difference of the magmatic heat output, which could serve as a prediction of the spatial volcanic activity variations, we find that the largest fluctuation amplitudes result from models that obtain an average maximum mantle temperature just above the solidus: For Model A a fluctuation of 84% around the average volcanic activity is possible, which should be detectable in a long time-series of observations. The maximum possible fluctuation for Model B (13%) would be difficult to detect. Current observations show Io's volcanic centre to be 30°-60° away from the sub- and anti-Jovian point (Hamilton et al., 2013). All of our resulting magmatic heat output patterns corresponding to a relative measure of the volcanic activity are symmetric towards Io's 0° W/E longitudinal plane independent of the varied parameters. Thus, based on our modelling approach it is not possible to favour one of the investigated end-member models for Io's interior.

The most crucial components of the modelling are the blurring of the produced heat and the separate, angle-wise estimation of the maximum mantle temperature using the scaling law of Vilella and Kaminski (2017) designed for a global convective system. A comparison between the scaling law of Vilella and Kaminski (2017) and three-dimensional, numerical modelling results by Laneuville et al. (2013) show that a large-scale anomaly, i.e. a differently heated hemisphere of the Moon, maintains its individual steady-state solution obtained by the

scaling law. This supports the validity of our model approach as we analyse only large-scale patterns comparable to the investigated anomaly. In addition to that, any lateral variations of the produced heat are already softened by the applied blurring (Section 3.2) before we apply the scaling law to approximate the temperature field. Furthermore, we assume that the used scaling law for a melt-free convective system is not affected by magma and that for any radial profile the heat transported by melt is proportional to the heat produced by tidal dissipation.

We only investigate large-scale patterns that are caused directly by tidal heating. The actual signature on Io's observable volcanic distribution is also influenced by structural and compositional inhomogeneities of Io's interior and crust. In particular mantle convection, featuring up-streams and down-streams, is a source of small-scale temperature heterogeneities. In a convecting medium up-streams occur more likely above areas with high temperatures or increased heating. However, our approach does not consider that Io's heating pattern (Fig. 4) may therefore facilitate certain convection schemes of up- and down-streaming patterns as suggested by Ross et al. (1990) and Tyler et al. (2015).

Any tidally induced feedbacks (secondary effects) of short- and long-wavelength patterns of the rheology on the heating pattern and convection scheme are not included in the model. For example, the lateral differences in the melt fraction and lid thickness (Fig. 6) eventually result in a different dissipation pattern than retrieved from our initial spherically symmetric rheological models. Han and Showman (2010) investigated this feedback and found that the tidal perturbation in a medium with temperature anomalies produces a heating pattern with small-scale features. In particular the strong boundary-focused manner of the asthenosphere-heating (Fig. 4) would be suppressed (Bierson and Nimmo, 2016). In addition, areas within the asthenosphere containing both solid and fluid material could be subject to a local and strong dissipative mechanism as suggested by e.g. Keszthelyi et al. (2007) and Tyler et al. (2015), thereby further increasing local heat production anomalies.

Despite the model uncertainties discussed above we conclude that tidal dissipation has a quantifiable effect on Io's lateral long-wavelength structure. Four interior properties determine whether the heating pattern becomes visible on Io's surface: The initial heating pattern itself, the heat transport mechanism, and the thickness and viscosity of the upper convective layer. Our results indicate that the assumption of a well-mixed interior is violated for a large number of model variables. That is why three-dimensional modelling approaches are necessary both for the computation of Io's tidal dissipation pattern and for the computation of Io's thermal heat transport. Our model based on finite elements can further be used for an extended investigation of Io's volcanic activity pattern resulting from any arbitrary or tidally induced three-dimensional rheological structure, or for investigating tidally heated exoplanets and exomoons.

Acknowledgement

This research has been financed by the User Support Programme Space Research, a program of the Netherlands Organization for Scientific Research, under the project number ALW-GO/15-07. The authors thank C.J. Bierson and K. Vilella for their constructive and useful suggestions on the manuscript. Further, the authors would like to thank Hermes Jara-Orué for helpful discussions.

Appendix A. Correction of mantle temperature distribution

Before we are able to estimate the melt fraction we need to correct the mantle temperature distribution for the temperature dependence of the mantle viscosity. To find the corrected distribution of the maximum temperature at the bottom of the thermal boundary layer we include a laterally varying mantle viscosity distribution. The mantle viscosity distribution $\eta_{con}(\theta,\phi)$ is a function of the maximum mantle temperature $T_{m,i}(\theta,\phi)$ and the initially given reference mantle viscosity $\overline{\eta}_{con}$. It is given by

$$\eta_{con}(\theta,\phi) = \eta_0 \exp\left(\frac{E_a}{R_{gas}\, T_{m,i}(\theta,\phi)}\right), \tag{A.1}$$

where

$$\eta_0 = \overline{\eta}_{con} \exp\left(-\frac{E_a}{R_{gas}\, \overline{T}_{m,i}}\right), \tag{A.2}$$

and $\overline{T}_{m,i}$ is the global average of $T_{m,i}(\theta,\phi)$. We assume that the mean temperature of the whole mantle is not significantly smaller than the maximum temperature $T_{m,i}$ and follows the same variations with longitude and co-latitude. Next, we substitute Eqs. (A.2) and (A.1) into Eq. (22) and obtain

$$T_{m,i}(\theta,\phi) = b_1 \exp\left(\frac{b_2(\theta,\phi)}{T_{m,i}(\theta,\phi)}\right), \tag{A.3}$$

with

$$b_1 = \frac{E_a}{8R_{gas}}, \tag{A.4}$$

and

$$b_2(\theta,\phi) = \gamma_0 (a_f Q_{cc,i}(\theta,\phi))^{\frac{3}{8}} \eta_0^{\frac{1}{8}}. \tag{A.5}$$

Eq. (A.3) can be solved using the Lambert relation $\mathscr{W}_0$. The Lambert relation describes a set of functions providing solutions to equations where the variables are found in both the exponent and the base. We obtain our final equation for the maximum mantle temperature

$$T_{m,i}(\theta,\phi) = \frac{b_1}{\mathscr{W}_0\left(\frac{b_1}{b_2}\right)}. \tag{A.6}$$

Appendix B. Specifications and benchmark of the finite element model

To ensure that the numerical finite element models work adequately, we compare the total dissipated energy rates with the results obtained by the semi-analytical approach (Jara-Orué and Vermeersen, 2011; Sabadini et al., 2016). To get the total dissipated energy for the FE model we average over one orbital period (Eq. (5)) and interpolate all nodes of the same sub-layer to an equiangular grid and integrate radially with the midpoint Riemann sum taking the spherical geometry into account. The values for the total heat production for the semi-analytical approach and FE of Model A and Model B are given in Table B.1.

To capture the entire dissipated power in Io's asthenosphere, a dense grid in radial direction is required. For Model A the asthenosphere is divided into 11 sub-layers to be able to capture the boundary focussed dissipation and the mantle is divided in 7 sub-layers. In Model B the asthenosphere and the mantle are divided in 8 and 10 sub-layers, respectively. The lateral mesh size for each layer in the mantle and crust is set to 2° at Io's surface and 4° for the core. The mesh for Model B is shown in Fig. B.1. Seven iterations are required for the models to converge to their final solution including the effect of self-gravitation (Section 2.2). A time sampling of 12 steps per one Io orbit is deemed sufficient, as the resulting total heat production rate $\dot{E}_{total}$ does not change significantly for a higher sampling rate. The effects of initializing the model are shown to be negligible after the first orbital cycle for the interior models used here. Due to Io's short tidal period of less than two days the deformation amplitude as well as the stress amplitudes are controlled by the elastic response of the body. The eigenmodes of both visco-elastic models, Model A and Model B, are either of small strength or have periods that are much longer than the forcing period. Hence, we set $\tau = P_{orbit}$ for computing the dissipation with Eq. (5).

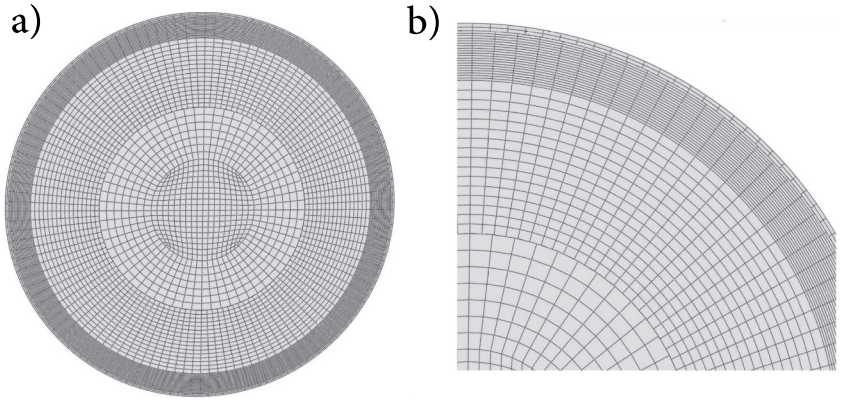

Fig. B.1. Mesh of Model B. a) Equatorial cut, b) close-up view of mesh for the asthenosphere, mantle, and crust.

The final relative residuals (Table B.1) between the semi-analytical model and the numerical model are below 4%. Large parts of this error are expected to occur at the asthenosphere boundaries. 1) Numerical inaccuracies in the stress calculation may arise due to large lateral displacements within the asthenosphere. 2) The radial discretization of the finite element model is crucial because the heating function varies over several orders of magnitudes towards the boundaries of the asthenosphere as described by Beuthe (2013) and Tackley (2001). However, the estimation of Io's total heat production rate is afflicted with inaccuracies (Lainey et al., 2009) and several other aspects of modelling such as Io's unknown heterogeneous rheology introduce much larger uncertainties. Thus, the accuracy of the results is deemed to be sufficient to be used for our further calculations.

Table B.1
Total heat dissipation $\dot{E}_{total}$ and total average heat flux $\overline{Q}$ for Model A and Model B resulting from the finite element method. The relative errors are calculated with respect to the given reference values given in the literature (Lainey et al., 2009).

Parameter	Reference	Model A	Model B
$\dot{E}_{total}$	$9.33 \cdot 10^{13}$ W	$9.02 \cdot 10^{13}$ W	$9.07 \cdot 10^{13}$ W
$\overline{Q}$	2.24 W m^{-2}	2.15 W m^{-2}	2.16 W m^{-2}
Relative error	–	3.4%	2.8%

Appendix C. Variation of Rayleigh-Roberts number

In Fig. C.1 we present the variation of the average Rayleigh-Roberts number as a function of the heat flux fraction $\overline{f}_{cc}$ and the reference mantle viscosity $\overline{\eta}_{con}$. It can be seen that the Rayleigh-Roberts number varies over more than several order of magnitude for Model A and B.

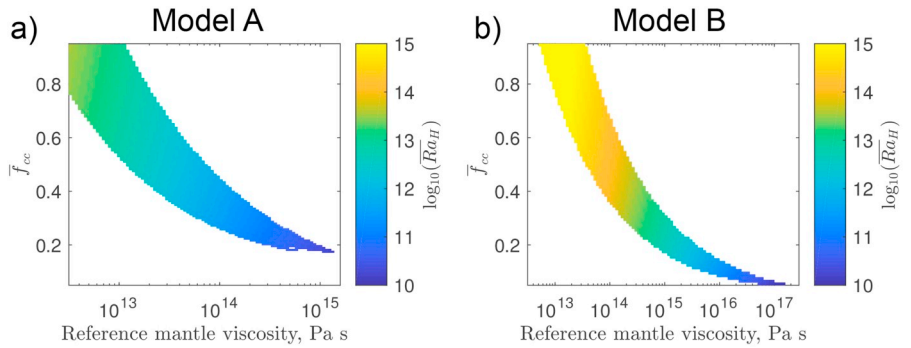

Fig. C.1. Globally averaged Rayleigh-Roberts number as a function of the heat flux fraction $\overline{f}_{cc}$ and the reference mantle viscosity $\overline{\eta}_{con}$ for Model A and Model B.

References

Anderson, J.D., Jacobson, R.A., Lau, E.L., Moore, W.B., Schubert, G., 2001. Io's gravity field and interior structure. Journal of Geophysical Research: Planets 106, 32963–32969.

Běhounková, M., Tobie, G., Choblet, G., Čadek, O., 2010. Coupling mantle convection and tidal dissipation: applications to Enceladus and Earth-like planets. Journal of Geophysical Research: Planets 115, E09011.

Běhounková, M., Tobie, G., Choblet, G., Čadek, O., 2011. Tidally induced thermal runaways on extrasolar Earths: impact on habitability. The Astrophysical Journal 728, 89–95.

Beuthe, M., 2013. Spatial patterns of tidal heating. Icarus 223, 308–329.

Bierson, C., Nimmo, F., 2016. A test for Io's magma ocean: modeling tidal dissipation with a partially molten mantle. Journal of Geophysical Research: Planets 121, 2211–2224.

Carr, M.H., 1986. Silicate volcanism on Io. Journal of Geophysical Research: Solid Earth 91, 3521–3532.

Castillo-Rogez, J.C., Efroimsky, M., Lainey, V., 2011. The tidal history of Iapetus: spin dynamics in the light of a refined dissipation model. Journal of Geophysical Research: Planets 116 (E09008).

Davies, A.G., Keszthelyi, L.P., Harris, A.J., 2010. The thermal signature of volcanic eruptions on Io and Earth. J. Volcanol. Geotherm. Res. 194, 75–99.

Davies, A.G., Veeder, G.J., Matson, D.L., Johnson, T.V., 2015. Map of Io's volcanic heat flow. Icarus 262, 67–78.

Deschamps, F., Yao, C., Tackley, P.J., Sanchez-Valle, C., 2012. High Rayleigh number thermal convection in volumetrically heated spherical shells. Journal of Geophysical Research: Planets 117.

Efroimsky, M., 2012. Tidal dissipation compared to seismic dissipation: in small bodies, Earths, and super-Earths. Astrophys. J. 746, 150–169.

Elder, C.M., 2015. The Effects of Melt on Impact Craters on Icy Satellites and on the Dynamics of Io's Interior, Dissertation. The University of Arizona.

Fischer, H.J., Spohn, T., 1990. Thermal-orbital histories of viscoelastic models of Io (J1). Icarus 83, 39–65.

Frouard, J., Efroimsky, M., 2017. Tides in a body librating about a spin–orbit resonance: generalisation of the Darwin–Kaula theory. Celest. Mech. Dyn. Astron. 129, 177–214.

Grasset, O., Parmentier, E., 1998. Thermal convection in a volumetrically heated, infinite Prandtl number fluid with strongly temperature-dependent viscosity: implications for planetary thermal evolution. Journal of Geophysical Research: Solid Earth 103, 18171–18181.

Hamilton, C.W., Beggan, C.D., Still, S., Beuthe, M., Lopes, R.M., Williams, D.A., Radebaugh, J., Wright, W., 2013. Spatial distribution of volcanoes on Io: implications for tidal heating and magma ascent. Earth Planet. Sci. Lett. 361, 272–286.

Han, L., Showman, A.P., 2010. Coupled convection and tidal dissipation in Europa's ice shell. Icarus 207, 834–844.

Hanyk, L., Matyska, C., Yuen, D.A., 2005. Short time-scale heating of the Earth's mantle by ice-sheet dynamics. Earth, Planets and Space 57, 895–902.

Hirschmann, M.M., 2000. Mantle solidus: experimental constraints and the effects of peridotite composition. Geochem. Geophys. Geosyst. 1 (2000GC000070).

Hu, H., Wal, W., Vermeersen, L., 2017. A numerical method for reorientation of rotating tidally deformed viscoelastic bodies. Journal of Geophysical Research: Planets 122, 228–248.

Hussmann, H., Spohn, T., 2004. Thermal-orbital evolution of Io and Europa. Icarus 171, 391–410.

Jara-Orué, H.M., Vermeersen, B.L., 2011. Effects of low-viscous layers and a non-zero obliquity on surface stresses induced by diurnal tides and non-synchronous rotation: the case of Europa. Icarus 215, 417–438.

Katz, R.F., Spiegelman, M., Langmuir, C.H., 2003. A new parameterization of hydrous mantle melting. Geochem. Geophys. Geosyst. 4, 1–19.

Kaula, W.M., 1964. Tidal dissipation by solid friction and the resulting orbital evolution. Rev. Geophys. 2, 661–685.

Keszthelyi, L., Jaeger, W., Milazzo, M., Radebaugh, J., Davies, A.G., Mitchell, K.L., 2007. New estimates for Io eruption temperatures: implications for the interior. Icarus 192, 491–502.

Khurana, K.K., Jia, X., Kivelson, M.G., Nimmo, F., Schubert, G., Russell, C.T., 2011. Evidence of a global magma ocean in Io's interior. Science 332, 1186–1189.

Kirchoff, M.R., McKinnon, W.B., Schenk, P.M., 2011. Global distribution of volcanic centers and mountains on Io: control by asthenospheric heating and implications for mountain formation. Earth Planet. Sci. Lett. 301, 22–30.

de Kleer, K., de Pater, I., 2016. Spatial distribution of Io's volcanic activity from near-IR adaptive optics observations on 100 nights in 2013–2015. Icarus 280, 405–414.

Lainey, V., Arlot, J.E., Karatekin, Ö., Van Hoolst, T., 2009. Strong tidal dissipation in Io and Jupiter from astrometric observations. Nature 459, 957–959.

Laneuville, M., Wieczorek, M., Breuer, D., Tosi, N., 2013. Asymmetric thermal evolution of the moon. Journal of Geophysical Research: Planets 118, 1435–1452.

Langseth, M.G., Keihm, S.J., Peters, K., 1976. Revised lunar heat-flow values. In: Lunar and Planetary Science Conference Proceedings, pp. 3143–3171.

Limare, A., Vilella, K., Di Giuseppe, E., Farnetani, C., Kaminski, E., Surducan, E., Surducan, V., Neamtu, C., Fourel, L., Jaupart, C., 2015. Microwave-heating laboratory experiments for planetary mantle convection. J. Fluid Mech. 777, 50–67.

Lissauer, J.J., De Pater, I., 2013. Fundamental Planetary Science: Physics, Chemistry and Habitability. Cambridge University Press.

Makarov, V.V., Efroimsky, M., 2014. Tidal dissipation in a homogeneous spherical body. II. Three examples: Mercury, Io, and Kepler-10 b. Astrophys. J. 795, 7–16.

McEwen, A.S., Keszthelyi, L., Spencer, J.R., Schubert, G., Matson, D.L., Lopes-Gautier, R., Klaasen, K.P., Johnson, T.V., Head, J.W., Geissler, P., Fagents, S., Davies, A.G., Carr, M.H., Breneman, H.H., Belton, M.J.S., 1998. High-temperature silicate volcanism on Jupiter's moon Io. Science 281, 87–90.

Moore, W., 2003. Tidal heating and convection in Io. Journal of Geophysical Research: Planets 108, 1–6.

Moore, W.B., 2001. The thermal state of Io. Icarus 154, 548–550.

Moore, W.B., Schubert, G., Anderson, J.D., Spencer, J.R., 2007. The interior of Io. In: Io After Galileo. Springer, pp. 89–108.

Ojakangas, G.W., Stevenson, D.J., 1989. Thermal state of an ice shell on Europa. Icarus 81, 220–241.

O'Reilly, T.C., Davies, G.F., 1981. Magma transport of heat on Io: a mechanism allowing a thick lithosphere. Geophys. Res. Lett. 8, 313–316.

Parmentier, E., Sotin, C., 2000. Three-dimensional numerical experiments on thermal convection in a very viscous fluid: implications for the dynamics of a thermal boundary layer at high Rayleigh number. Phys. Fluids 12, 609–617.

Parmentier, E., Sotin, C., Travis, B., 1994. Turbulent 3-D thermal convection in an infinite Prandtl number, volumetrically heated fluid: implications for mantle dynamics. Geophys. J. Int. 116, 241–251.

Peale, S.J., Cassen, P., Reynolds, R.T., 1979. Melting of Io by tidal dissipation. Science 203, 892–894.

Renaud, J.P., Henning, W.G., 2018. Increased tidal dissipation using advanced rheological models: implications for Io and tidally active exoplanets. Astrophys. J. 857, 1–29.

Roberts, J.H., Nimmo, F., 2008. Tidal heating and the long-term stability of a subsurface ocean on Enceladus. Icarus 194, 675–689.

Roberts, P., 1967. Convection in horizontal layers with internal heat generation. J. Fluid Mech. 30, 33–49.

Ross, M., Schubert, G., Spohn, T., Gaskell, R., 1990. Internal structure of Io and the global distribution of its topography. Icarus 85, 309–325.

Roth, L., Saur, J., Retherford, K.D., Blöcker, A., Strobel, D.F., Feldman, P.D., 2017. Constraints on Io's interior from auroral spot oscillations. J. Geophys. Res. Space Physics 122, 1903–1927.

Sabadini, R., Vermeersen, B., Cambiotti, G., 2016. Rotational dynamics of viscoelastic planets: linear theory. In: Global Dynamics of the Earth: Applications of Viscoelastic Relaxation Theory to Solid-Earth and Planetary Geophysics. Springer, pp. 87–148.

Schubert, G., Turcotte, D.L., Olson, P., 2001. Mantle Convection in the Earth and Planets. Cambridge University Press.

Segatz, M., Spohn, T., Ross, M., Schubert, G., 1988. Tidal dissipation, surface heat flow, and figure of viscoelastic models of Io. Icarus 75, 187–206.

Spohn, T., 1991. Mantle differentiation and thermal evolution of Mars, Mercury, and Venus. Icarus 90, 222–236.

Stevenson, D.J., McNamara, S.C., 1988. Background heatflow on hotspot planets: Io and Venus. Geophys. Res. Lett. 15, 1455–1458.

Tackley, P.J., 2001. Convection in Io's asthenosphere: redistribution of nonuniform tidal heating by mean flows. Journal of Geophysical Research: Planets 106, 32971–32981.

Tackley, P.J., Schubert, G., Glatzmaier, G.A., Schenk, P., Ratcliff, J.T., Matas, J.P., 2001. Three-dimensional simulations of mantle convection in Io. Icarus 149, 79–93.
Tobie, G., Mocquet, A., Sotin, C., 2005. Tidal dissipation within large icy satellites: applications to Europa and Titan. Icarus 177, 534–549.
Tosi, N., Godolt, M., Stracke, B., Ruedas, T., Grenfell, J.L., Höning, D., Nikolaou, A., Plesa, A.C., Breuer, D., Spohn, T., 2017. The habitability of a stagnant-lid Earth. Astronomy & Astrophysics 605, A71.
Turtle, E.P., Jaeger, W.L., Schenk, P.M., 2007. Ionian mountains and tectonics: insights into what lies beneath Io's lofty peaks. In: Io After Galileo. Springer, pp. 109–131.
Tyler, R.H., Henning, W.G., Hamilton, C.W., 2015. Tidal heating in a magma ocean within Jupiter's moon Io. Astrophys. J. Suppl. Ser. 218, 22.
Veeder, G.J., Davies, A.G., Matson, D.L., Johnson, T.V., Williams, D.A., Radebaugh, J., 2015. Io: heat flow from small volcanic features. Icarus 245, 379–410.
Vilella, K., Kaminski, E., 2017. Fully determined scaling laws for volumetrically heated convective systems, a tool for assessing habitability of exoplanets. Phys. Earth Planet. Inter. 266, 18–28.
Wu, P., 2004. Using commercial finite element packages for the study of earth deformations, sea levels and the state of stress. Geophys. J. Int. 158, 401–408.
Yoder, C.F., Peale, S.J., 1981. The tides of Io. Icarus 47, 1–35.